Theoretical and Numerical Studies of Inelastic Impacts of Elastic Materials

A doctoral dissertation presented to the Graduate School of Human and Environmental Studies of Kyoto University for the Degree of Doctor of Philosophy.

by
Hiroto Kuninaka
March 2004

Abstract

The theoretical and numerical analyses of inelastic impacts of elastic materials are presented. We construct the two-dimensional impact model based on the spring-mass model and simulate normal and oblique impacts to investigate how initial condition affects coefficients of normal and tangential restitution. At first, we demonstrate the low speed impact of the elastic disk on the structureless wall. In this case, our numerical results of the relation between the colliding speed and the compressive force could not be reproduced by the quasi-static theory while the relation between the duration and the colliding speed could reproduced by two-dimensional Hertzian impact theory. In addition, in high speed impacts, we found the abrupt decrease of the coefficient of restitution(COR) by the plastic deformation of the model around the critical impact velocity which seems to be a simple linear function of temperature. We also demonstrate the normal impact of an elastic disk on an elastic wall, in which COR decreases as the thickness of the wall increases.

In addition, we carry out the simulation of the oblique impact. Using a two-dimensional random lattice model of an elastic disk and an elastic wall, we investigate the relation between the coefficient of tangential restitution and the incident angle. Our numerical results can be well reproduced by the present phenomenological theory of oblique impacts. Finally, we demonstrate that the coefficient of normal restitution can exceed unity and have a peak at an incident angle in our simulation of the oblique impact. Similar tendency is also observed in the experiment by Louge and Adams(2002), in which COR can be expressed as a linear function of the magnitude of the tangent of the incident angle. We explain our numerical results based upon the phenomenological theory.

Biographical Sketch

1973 Born in Naha city, Okinawa, Japan

Education

l997 B. A., Yokohama National University, Japan
2000 M. of Human and Environmental Studies, Kyoto University, Japan
2004 Ph.D, Kyoto University, Japan

Thesis

- Bachelor Thesis
  "The numerical analysis of anharmonic oscillator"
  (1997, Yokohama National University)
- Master Thesis
  "The analysis of the coefficient of restitution of two-dimensional elastic disks"
  (2000, Kyoto University)
- Ph.D Thesis
  "Theoretical and numerical studies of inelastic impacts of elastic materials"
  (2004, Kyoto University)

Acknowledgement

First of all, I am very grateful to the supervisor of this dissertation, Prof. Hisao Hayakawa, for suggesting me the exciting and challenging problem. For past 6 years, I have learnt a lot from his serious attitude to physics and really enjoyed collaborative works with him.

I would like to thank all the present members of the statistical physics group, Prof. Hiroyuki Tomita, Prof. Shinji Takesue, Prof. Mitsusada Sano, Kim Hyeon-Deuk, Chiyori Urabe, Atsushi Kawarada, Tetsuya Mitsudo, Nobuyoshi Ariga, and Dr. Aiguo Xu as well as the old members, Shigeaki Wada, Dr. Kengo Ichiki, Toshiyuki Ayukawa, Naoto Yajima, and Prof. Sanjay Puri. This work has been carried out through their support and encouragement.

I appreciate all the members of my dissertation committee, Prof. Hiroyuki Tomita, Prof. Hisao Hayakawa, Prof. Shinji Takesue, Prof. Masaaki Sakagami, and Prof. Yoshihisa Miyamoto for reviewing my manuscripts and giving me valuable comments.

I am grateful to Dr. Yoshimi Tanaka of Toyama Prefectural University, Dr. Akinori Awazu of University of Tokyo, Dr. Masaharu Isobe of Nagoya Institute of Technology, Dr. So Kitsunezaki of Nara Women's University, Shin-ichiro Nagahiro, Masayasu Noguchi, Prof. Shin-ichi Sasa of University of Tokyo, and Prof. Yoshinori Hayakawa of Tohoku University for their valuable comments and fruitful discussions. Prof. Tsuyoshi Mizuguchi, Prof. Hiraku Nishimori, and Prof. Hiroaki Daido of Osaka Prefecture University gave me an opportunity of my presentation at their seminar on October of 2003. I really appreciate their valuable comments and discussions. I would like to thank Prof. Michel Y. Louge of Cornell University. His presentation regarding his impact experiments in our small workshop at Kyoto University on July of 2002 was really impressive and became the basis for our recent works. A part of numerical simulation was carried out using the excellent Fortran code of Delaunay triangulation by Prof. Kokichi Sugihara of University of Tokyo. Also, I would like to thank Prof. Ken Sasaki of Yokohama National University who was my adviser at undergraduate course and invited me to research works of physics.

Parts of numerical computation in this work were carried out at Yukawa In-

stitute Computer Facility. This work is partially supported by Hosokawa Powder Technology Foundation, Inamori Foundation, and Grant-in-Aid of Ministry of Education, Science and Culture, Japan (Grant No. 15540393)

Finally, I am very grateful to my parents, Hiroyuki Kuninaka and Nobuko Kuninaka, and my grand parents, Katsu Kuninaka and Kanriki Kuninaka, for their support and love.

Contents

1 General introduction **1**
- 1.1 History of impact studies . . . 3
- 1.2 Theoretical approach to impact problems: quasi-static theory . . . 5
- 1.3 Numerical approach . . . 7
- 1.4 The composition of the dissertation . . . 12

2 Normal impact of an elastic disk on a wall without internal structure **15**
- 2.1 Models . . . 15
  - 2.1.1 Model A . . . 16
  - 2.1.2 Model B . . . 17
  - 2.1.3 Parameters in both models . . . 18
- 2.2 Results . . . 19
  - 2.2.1 Simulation at $T = 0$ . . . 19
  - 2.2.2 Simulation at finite T . . . 23
- 2.3 Discussion . . . 25
  - 2.3.1 Application of the conventional theory of plastic deformation to 2D impacts . . . 26
  - 2.3.2 Realistic systems . . . 30
- 2.4 Conclusion of this chapter . . . 31

3 The coefficient of restitution as a function of wall thickness **33**
- 3.1 Introduction . . . 33
- 3.2 Model . . . 34
- 3.3 Simulation result . . . 35
- 3.4 Conclusion remarks . . . 35

4 Oblique impact of a random lattice model **37**
- 4.1 Model . . . 37

4.2 Walton's collision model 42
4.3 Results 42
4.4 Discussion and conclusion 47

5 Oblique impact of an elastic disk on a soft wall 49
5.1 Model 49
5.2 e vs. Ψ_1 52
5.3 μ vs. Ψ_1 54
5.4 Discussion and conclusion 55

6 General discussion 59
6.1 Comparison with the Hertzian contact theory 61
6.2 Comparison with quasi-static theory 62

7 General conclusion 65

A Walton's collision model 67

B The Theoretical description of the oblique impact 71
B.1 The equation of motion 71
B.2 Velocity and force of the contact point 73
B.2.1 Normal components of velocity and force 74
B.2.2 Tangential components of velocity and force 74
B.2.3 Obtaining the transition time, t_1 75
B.3 Three regimes of the angle of incidence 75

C Poisson's ratio for a square lattice system with next-nearest neighbor interaction 79

D Contact of a hard disk on an elastic half-space 81

E The Chronological table of impact studies 85

List of Figures

1.1 Schematic figure of triangular lattice model. 8
1.2 The random lattice disk with rough surface. 10
1.3 Interaction between surface particles of the disk and the wall. . . . 11

2.1 The disk of model A or B approaching to the potential wall. 16
2.2 Coefficient of restitution for normal collision of the Model A and Model B as a function of impact velocity, where $c = \sqrt{E/\rho}$ with the Young's modulus E and the density ρ. 437 and 1189 modes are chosen for model B. 20
2.3 The comparison of the Hertzian force in Eq.(1.7) with our simulation at $v_i = 0.01c$ (a) and $v_i = 0.001c$(b) at $T = 0$ in model B. F_{tot} is the total force originated from the interaction with a wall. . 21
2.4 The time evolution of the center of mass of the elastic disk under the compression by $g = 0.01c^2/R$ (model B with N=437). Here the dimensionless time is measured by R/c and the position of C.M. (center of mass) is measured by the diameter of the disk (2R). Simulation is performed at the finite temperature $T = 10^{-8}Mc^2$ and is averaged over 20 independent samples which start from initial condition satisfying the Gibbs distribution. . . . 22
2.5 The plot of contact time versus the impact velocity. R represents the radius of the disk, in which $R = 40$,60,70 and 80 correspond to the number of mass points 5815, 13057, 17761 and 23233, respectively. The dotted line is fitting curve based on the quasi-static theory. 24
2.6 The average shift of COR at finite temperature $T = 10^{-8}Mc^2$ as a function of the impact velocity in model B with $N = 437$. 25
2.7 The standard deviation of COR $\sqrt{(e- < e >)^2}$ at $T = 10^{-8}Mc^2$ as a function of the impact velocity v_i via model B with $N = 437$. 26

2.8 The relation the coefficient of restitution and the impact velocity rescaled by the critical velocity for each temperature. Curves are plotted in the log-log scale. The temperature is scaled by $T_0 = mc^2$ with the mass of the mass points m. Note that the error bars are plotted only in the case $T/T_0 = 0.03$ but is the same order even at other T (model A). 27
2.9 The plot of the initial temperature and the critical velocity causing the plastic deformation. $v_{cr}/c = a(T/T_0) + b$ is the fitting curve line from the data between $T/T_0 = 0.02$ and 0.05 (model A). . . . 28
2.10 (a) Plastic deformation of model A with $v_i = 0.22c$ at $T = 0.03mc^2$. The solid line represents the initial circle. The points in a circle are positions of the mass points after the collision. The deformation is asymmetric because of the velocity distribution at the initial stage. (b) All the mass points of the disk initially consist of triangular lattice. When the deformation occurs, it is possible that the configurations of mass points (points in figure) locally change like this figure. Note that these two configurations are energetically equivalent. 29

3.1 Impact model consisted from an elastic disk and an elastic wall. . 34
3.2 The relation between the normal impact velocity of the disk and the coefficient of restitution. Each curve has different value of D_d/T_w. The curve labeled modelA is the result in the situation when the wall has no internal degrees of freedom. 36

4.1 The schematic figure of a collision of a disk with a wall. 38
4.2 The elastic disk and wall consisted of random lattice system. . . . 39
4.3 The bands of random lattice (a) before and (b) after stretch. 40
4.4 The schematic figures of (a) triangular lattice disk and (b) square lattice disk. 41
4.5 The relation between cotangent of angle of incidence γ and COR e. 43
4.6 The relation between cotangent of angle of incidence γ and β. Cross points are the results of the random lattice disk. Stars are the result when the random disk has no roughness. Plus points are the results of the triangular lattice disk. Dashed and dot-dash lines are Eq.(4.3) 44

4.7 The relation between $\cot\gamma$ and β. Cross points are the numerical results of the random lattice model. Solid line is the theoretical curve. 46

5.1 The elastic disk and the elastic wall consisted of random lattice. . 50
5.2 Numerical and theoretical results of the relation between Ψ_1 and COR. 51
5.3 The schematic figure of a hard disk sliding on a soft wall. x coordinates of both ends of the contact area AB are $x = x_a$ and $x = x_b$. 52
5.4 Numerical and theoretical results of the relation between Ψ_1 and μ. 54
5.5 The relation between Ψ_1 and μ in the case of hard wall. 56
5.6 The relation between Ψ_1 and μ in the case of $\zeta = 0$ and $\eta\rho = 0.014c/R$ in Eq.(5.10). 57
5.7 Numerical and theoretical results of the relation between Ψ_1 and e when e^α is not a constant. 58

6.1 The disk is in contact with a potential wall 62
6.2 The relation between the compressive force and the macroscopic deformation 63
6.3 The relation between impact velocity and coefficient of restitution. 64

A.1 The schematic figure of binary collision. 68

B.1 The schematic figure of the disk and the wall. A cross in a circle represents a center of mass of each body. 72

List of Tables

B.1 Normal displacement, velocity, force, and impulse 74

List of notations

a	radius of contact area
a_0	a constant
a^*	maximum value of contact area
b	a constant
c	velocity of one-dimensional elastic wave
d_0	lattice constant
e	the coefficient of restitution(COR)
e_*	energetic coefficient of restitution
$f(x)$	shape of contact area
g	dimensionless external field
h	macroscopic deformation
h^*	maximum value of macroscopic deformation
k	spring constant
k_a, k_b	spring constants
k_1, k_2	spring constants for an elastic wall of square lattice (k_1: nearest neighbour, k_2: next-nearest neighbour)
$k_a^{(i)}, k_b^{(i)}$	spring constants($i = d$(disk) or w(wall))
$\hat{k}_r$	radius of gyration for center of mass
l	mode index
l_c	contact length
l_s	distance between surface particle of a disk and a spring of wall surface
l_{th}	threshold
m_{eff}	reduced mass
m_1, m_2	mass of spheres 1 and 2
n	mode index
$\mathbf{n}$	normal unit vector to a wall
$\mathbf{n}_s$	normal unit vector to a spring
n_x, n_y	components of normal unit vector
$\mathbf{n}_y$	normal unit vector in y direction
p_r	pressure
$\mathbf{p}$	impulse
$p(x)$	pressure distribution
r	scaled parameter, radial coordinate
$r_i, r_i^{'}$	position vectors from centers of mass to contact point

$\mathbf{r}_i$	position of i-th particle
$\mathbf{r}_p$	position of particle
s	scaled parameter
t	time
t_1	time of transition from initial stick to sliding
t_2	time of transition from sliding to stick
t_3	time of transition from stick to sliding
t_c	time when compression period terminates
t_f	time when restitution period terminates
$\mathbf{t}$	tangential unit vector
$\mathbf{u}$	elastic deformation field in polar coordinate
$u_r(r,\phi), u_\phi(r,\phi)$	radial and normal components of elastic deformation
$\mathbf{v}(t)$	velocity of center of mass at time t
$v_n(t), v_t(t)$	normal and tangential components of velocity of center of mass at time t
v	impact speed of center of mass
$\mathbf{v}$	impact velocity of center of mass
v_{cr}	critical speed
$v_n, v_n^{'}$	normal components of relative velocities of center of mass before and after collision
$v_t, v_t^{'}$	tangential components of relative velocities of center of mass before and after collision
$v_n^{(c)}, v_n^{(c)'}$	normal components of relative velocities of contact point before and after collision
$v_t^{(c)}, v_t^{(c)'}$	tangential components of relative velocities of contact point before and after collision
v_{th}	thermal speed
x	x coordinate
x_a, x_b	x coordinates of both sides of contact area
x_c	coordinates of contact point
x_c^*	scaled parameter
x_i, y_i	position of i-th particle
$\mathbf{x_{ij}}$	stretch
y	y coordinate
y_c	y coordinates of contact point
$y_0(t)$	position of center of mass at time t
z	depth coordinate

A	free constant
$A_{n,l}$	constant
A_Y	constant
B	free constant
$B_{n,l}$	constant
$C_{n,l}$	constant
$D, D^{'}$	constants
D_d	diameter of a disk
E	Young's modulus
E_1, E_2	Young's modulus of spheres 1 and 2
E_*	effective Young's modulus($= E/1 - \nu^2$)
F^*	maximum force
F_{dis}	dissipative force
F_{el}	elastic force
F_{tot}	total force
$F(l)$	force as a function of distance l
H	Hamiltonian
I	moment of inertia
$\mathbf{J}$	impulse
J_n, J_t	normal and tangential impulse
$J_t^{'}$	correction of tangential impulse
$J_n(x)$	n-th order Bessel function
$M, M^{'}$	masses
N	number of mass points
N_i	number of mass points connected to i-th mass point
$\mathbf{P}$	external force
$P_{n,l}$	canonical momentum(2D)
$\mathbf{P}_0$	momentum of center of mass
$Q_{n,l}$	canonical coordinate(2D)
R	radius of a disk
R_1, R_2	radii of spheres 1 and 2
$S_{n,l}$	constant
T	temperature
T_w	thickness of a wall
T_0	$= mc^2$
U	elastic energy
V_0	a constant

$V_{ij}(x)$	potential of spring
$W, W^{'}$	works

Greek letters

α	correction angle
β	coefficient of tangential restitution
β_x, β_z	inertia coefficients
β_Y	constant
β_0	maximum value of β
δ	standard deviation
ϕ	angle
η	square root of ratio of tangential to normal compliance
η_{dis}	viscosity coefficient
η_t	fitting parameter
γ	incident angle
γ_0	critical angle
κ	stiffness coefficient of spring element
κ_c	constant
$\tilde{\kappa}_c$	constant
μ	Amontons-Coulomb coefficient of limiting friction(dry friction)
μ_0	coefficient of friction in Walton's argument of oblique impacts
μ^{α}	coefficient of friction without surface deformation
ν	Poisson's ratio
ν_1, ν_2	Poisson's ratios of spheres 1 and 2
θ	step function
ρ	density
ω	tangential resonant frequency
τ	duration
τ_0	time scale of dissipation
ξ	argument
ζ	fitting parameter
ΔP	change of impulse

Δt	time step
Ω	normal resonant frequency
Ψ_1	tangent of incident angle, $\tan \gamma$

Chapter 1

General introduction

The object of the present dissertation is to investigate the relation between the initial condition of colliding material and its coefficients of both normal and tangential restitution theoretically with the aid of computer simulation. In this dissertation, we carry out numerical simulation of two-dimensional impacts of elastic material and compare the numerical results with early experimental results. In addition, we attempt to explain our numerical results by the phenomenological theories of impacts.

We can see many examples of impact around us. In microscopic level, atoms and molecules are colliding each other in atmosphere while in macroscopic level meteorites are colliding in cosmic space. Also in our daily life, we can see baseballs, billiard balls, hammers and nails, and so on. In the fields of mechanical engineering and sports science, it is important to control mechanical shock of impacts. For example, internal structure of balls and bats of baseball are designed to control rebound of balls. In the engineering of vehicle, chassis of cars is designed to avoid damage to passengers as possible in traffic accidents.

In general, theoretical prediction of post-collisional state of macroscopic colliding materials is difficult because actual collision occurs in finite duration accompanying deformation, fracture, sound emission, thermalization, and so on. In such a collision, a part of initial energy of colliding materials is distributed into some degrees of freedom during duration. We call such the collision as an inelastic collision. When we consider a physical process of collision from the viewpoint of energy dissipation, the following questions will arise naturally:

1. What is the dominant mechanism of energy dissipation?

2. How are post-collisional quantities decided from the initial condition of col-

liding material?

Because of difficulties in measuring physical quantities during impact process, many problems including above questions are left to be open.

To characterise post-collisional physical state, the coefficient of restitution(COR) is often used. The definition of COR e in normal collision is given by

$$e = -\frac{v_n^{'}}{v_n}, \tag{1.1}$$

where v_n and $v_n^{'}$ are the normal components of relative velocities of center of mass before and after collision, respectively. COR indicates the amount of energy dissipation of the colliding material because it is also defined by the square root of the ratio of translational energy before collision to that after collision. COR firstly appears in *Principia*[1] by Newton as the ratio of a rebound speed to a impact speed in normal collisions. Newton suggested that COR is independent of the size and the relative colliding speed of materials. However, it has been clarified that COR depends on the pre-collisional state of a colliding material in many experiments[2, 3, 4, 5, 6, 7, 8, 9, 10, 11, 12, 13, 14, 15, 16, 17]. Newton defined COR as just the ratio of the normal speed before collision to that after collision. However, if we want to know how COR is determined from the pre-collisional state, we need to investigate the process of energy dissipation because COR is determined through the process of energy dissipation in a finite duration. Clarifying the process of energy dissipation and the mechanism of determination of COR are important not only for engineering and science but also for elementary physics. COR plays an important role also in computer simulation of various fields of engineering. For example, in the fields of powder engineering, chemical engineering, civil engineering, and earth science, Distinct Element Method (DEM) is a popular simulation method[18] to describe behaviors of granular materials[19, 20, 21, 22, 23]. In DEM, COR is included as a function of phenomenological parameter. Clarifying the mechanism of determining COR will give the theoretical foundation of DEM and improve the precision of calculation.

The goal of our research is to specify the dominant mechanism of dissipation in impacts of materials with various kinetic states. In this dissertation, we will show numerical results of two-dimensional simulation of impacts of an elastic disk on an elastic wall and some theoretical analysis of the results.

1.1 History of impact studies

In this section, we review the history of impact studies. After the introduction of COR by Newton, many impact experiments were carried out to measure COR of various kinds of material. Hodgikinson carried out impact experiments of various kinds of materials and measured COR against some impact velocities[8]. In his paper[8], he referred to the decreasing tendency of COR against the increasing impact velocity though COR had been believed to be constant value. At the end of the 19th century, it became clear experimentally that COR systematically depends on the relative velocity of the colliding materials[10]. In the text book of Goldsmith[14], many experimental data of various kinds of materials about the relation between impact velocity and COR are shown. Generally, COR decreases as impact velocity increases. However, the behavior of COR for low impact velocity and that in high impact velocity are believed to be quite different. For example, Sondergaard *et al.* performed an impact experiment of ball bearings and glass spheres on lucite or aluminum plates and confirmed the dependency on the impact velocity as $e \propto v^{-1/4}$ in the high speed impact[15]. Later, physical mechanism of this behavior has been explained by the dimensional analysis[24, 25]. Kuwabara and Kono performed impact experiment of two pendulums [26]. They made two spheres of various materials (steel, glass, brass, and cork) collide each other with the low impact velocity $v = 0.5m/s$. Their experimental results may be consistent with their theoretical prediction $1 - e \propto v^{1/5}$ by the quasi-static argument.

On the other hand, the dependency of coefficient of tangential restitution on incident angle in oblique collisions was investigated both experimentally and theoretically. Coefficient of tangential restitution β is defined as

$$\beta = -\frac{v_t^{(c)'}}{v_t^{(c)}}, \tag{1.2}$$

where $v_t^{(c)}$ and $v_t^{(c)'}$ are tangential components of impact velocities of the contact point before and after collision, respectively. Maw *et al.* have formulated the theory of oblique impacts of elastic material[27, 28, 29]. They assumed normal and tangential force acting on a contact point of two contacting materials as linear springs with two different frequencies. The validity of the theory was confirmed by many experimental results [6, 28, 30].

Meanwhile, Walton gives a simple argument of oblique impacts by introducing three phenomenological parameters: the coefficient of normal restitution e, the coefficient of Coulomb's friction μ, and the maximum value of the coefficient

of tangential restitution β_0[31, 32]. Details of Walton's argument are shown in chapter 4 and appendix A. Experiments have supported that his characterization adequately captures the essence of binary collisions of metal spheres or collision of a metal sphere on a flat plate [4, 5, 6, 7].

Later, systematic investigation of COR in normal impacts with quasi-static theory was developed by Kuwabara and Kono[26]. They investigated COR for low speed impact by solving the equation of macroscopic deformation of colliding spheres taking into account the viscous motion among the internal degrees of freedom and derived the theoretical expression $1 - e \propto v^{1/5}$. Their theoretical results can reproduce their experimental results [26]. After their work, some papers about quasi-static theory have been published which are consistent with the results of Kuwabara and Kono[33, 34, 35, 36]. Brilliantov *et al.*[33] derived similar expression for time evolution of macroscopic deformation to that of Kuwabara and Kono and compared its results with the experimental results by Bridges *et al.* [2]. Also, Morgado and Oppenheim[34] derived similar expression for binary collision of two identical spheres from different approach and showed consistency to the results of Kuwabara and Kono. Thus, quasi-static theory is believed to capture the essence of low speed impact.

Recently, Gerl and Zippelius performed a two-dimensional simulation of collision of an elastic disk with an elastic wall[37]. Hayakawa and Kuninaka performed two-dimensional simulations and confirmed that elastic models including that of Gerl and Zippelius is not appropriate to characterize the quasi-static impact[38, 39, 40, 41]. Some discussions about this tendency will appear in this dissertation later. In addition, COR in oblique impacts has been investigated. While COR has been believed to be less than unity in most situations, it is recently reported that COR can exceed unity in oblique impacts in some experimental and numerical studies [30, 42, 43, 44]. In particular, Louge and Adams[30] reported that COR increases as a linear function of the magnitude of $\tan\gamma$ in the oblique impact of a hard aluminum oxide sphere on a thick elastoplastic plate with the incident angle γ. This novel and anomalous behavior of COR will be discussed in chapter 5. Apart from impacts between solids, impact experiments such as a sphere on a liquid surface[45], liquid marbles on flat surfaces[46], and a sphere on granular material[47] are also carried out recently.

1.2 Theoretical approach to impact problems: quasi-static theory

Here, we review quasi-static theory which is one of theoretical approaches to impact problems. We focus on the normal impact with low impact speed. As mentioned in the last section, in low speed impact, quasi-static theory is believed to be valid. Quasi-static theory is based on the Hertzian contact theory[48, 49, 50, 51]. Hertzian contact theory describes relative normal deformation of two spheres in contact while Mindlin theory describes relative tangential deformation [52, 53]. Here, we briefly review Hertzian contact theory[48, 49, 50, 51] firstly, and extend it to quasi-static theory.

Let us consider that two spheres with radii R_1 and R_2 are in contact under elastic force F_{el} each other. From Hertzian contact theory, the macroscopic deformation h and the radius of contact area a can be expressed as a function of F_{el} as

$$h = F_{el}^{2/3}\left[D^2\left(\frac{1}{R_1}+\frac{1}{R_2}\right)\right] \quad \text{and} \tag{1.3}$$

$$a = F_{el}^{1/3}\left[D\frac{R_1R_2}{R_1+R_2}\right], \tag{1.4}$$

where $D = (3/4)\left[(1-\nu_1^2)/E_1 + (1-\nu_2^2)/E_2\right]$, E_1 and ν_1 are Young's modulus and Poisson's ratio for sphere 1 and E_2 and ν_2 are for sphere 2. Thus, elastic energy U can be calculated by integrating F_{el} by h as

$$U = h^{5/2}\frac{2D}{5}\left[\frac{R_1R_2}{R_1+R_2}\right]^{1/2}. \tag{1.5}$$

Dynamic equation for a collision of two elastic spheres can be derived as

$$m_{eff}\frac{d^2h}{dt^2} + \frac{5}{4}\kappa_c h^{3/2} = 0, \tag{1.6}$$

where $\kappa_c = (4/5D)[R_1R_2/(R_1+R_2)]^{1/2}$, t is time, and $m_{eff} = 1/m_1 + 1/m_2$. Solving Eq.(1.6), we can calculate COR from the ratio of dh/dt after collision to that before collision. However, in elastic case, COR equals to unity according to energy conservation.

In the two-dimensional case, the relation between the macroscopic deformation of the center of mass h and the elastic force F_{el} is

$$h \simeq -\frac{F_{el}}{\pi E_*}\left\{\ln\left(\frac{4\pi E_* R}{F_{el}}\right) - 1 - \nu\right\}, \tag{1.7}$$

where $E_* = E/(1-\nu^2)$. If h is given, we can calculate numerically two-dimensional F_{el} from Eq.(1.7).

In quasi-static theory, total compression force is expressed by the sum of the elastic force F_{el} and the dissipative force F_{dis} which is introduced as a function proportional to dh/dt. Kuwabara and Kono considered F_{dis} comes from internal friction of spheres and obtained its explicit form as $F_{dis} = -(5/2)\tilde{\kappa}_c\sqrt{h}dh/dt$, where $\tilde{\kappa}_c = (4/5D^{'})\left[R_1R_2/R_1+R_2\right]^{1/2}$ and $D^{'}$ is a constant calculated from coefficient of viscosity associated with volume deformation and shear. The equation of the macroscopic deformation is given by

$$m_{eff}\frac{d^2h}{dt^2} + \frac{5}{4}\kappa_c h^{3/2} + \frac{5}{2}\tilde{\kappa}_c\sqrt{h}\frac{dh}{dt} = 0. \tag{1.8}$$

By solving this equation with adequate initial condition, they obtain the relation between e and initial speed v as

$$e \simeq 1 - 1.009 \times \frac{5}{2}\tilde{\kappa}_c\left(\frac{v}{\kappa_c^3 m_{eff}^2}\right)^{1/5}. \tag{1.9}$$

Note that the value of $1-e$ is proportional to $v^{1/5}$ [1]. Later, identical equations to Eq.(1.8) were derived in some studies from different approaches [33, 34, 35, 36].

In the two-dimensional case[37, 39], the total force may be given by

$$F_{tot} \simeq -\frac{\pi E_* h}{\ln(4R/h)} - \tau_0\frac{\pi E_*}{\ln(4R/h)}\frac{dh}{dt}, \tag{1.10}$$

where τ_0 represents the time scale for dissipation, when the deformation is small. Replacing the logarithmic term as a constant correction, the equation for elastic motion can be solved as in the three dimensional case. Thus, we may evaluate the duration t_f as

$$t_f \simeq \frac{\pi R}{c}\sqrt{\ln\frac{4c}{v}}, \tag{1.11}$$

where $c = \sqrt{E_*/\rho}$ and ρ are the compressive sound velocity and the density, respectively. We note that we adopt a bold approximation: $h^* \simeq vR\sqrt{(\rho/E_*)\ln(4R/h)} \sim vR/c$. Including dissipative force as before, this approximation gives

$$e \simeq \sqrt{1 - \frac{2\tau_0\pi E_*}{\rho R c\sqrt{\ln(4c/v)}}}. \tag{1.12}$$

[1] Recently, Hayakawa and Kuninaka[54] obtained same result by the analysis taking the effect of radiation of elastic waves into account [55, 56, 57, 58].

1.3 Numerical approach

As a numerical study to investigate the relation between COR and initial velocity, Gerl and Zippelius performed two-dimensional simulation with a continuum model[37]. Their simulation is mainly based on the mode expansion of an elastic disk under the force free boundary condition. They do not introduce any dissipative mechanism in the microscopic equation of motion of the disk. They solve Hamilton's equation determined by the elastic field and the repulsive potential to represent the collision of two disks. Their results show that COR decreases with increasing impact velocity and strongly depends on Poisson's ratio.

On the other hand, some studies about binary collision of two one-dimensional bars exist [59, 60, 61, 62, 63, 64]. In one-dimensional case, COR is believed to be equal to the ratio of the lengths of two colliding bars.

There exist some numerical studies of impact using FEM (Finite Element Method) which is used in the field of engineering [42, 65, 66, 67]. Lim and Stronge carried out 2D analysis of a cylinder colliding transversely against an elast-plastic half space using the finite element code, DYNA2D[65]. They showed that their numerical results can be reproduced by the theoretical result by Johnson[25]. It has been also reported that 3D FEM analysis can reproduce experimental data of binary collision of metal spheres[66].

Our numerical models are based on spring-mass models which are often used in physical modeling of deformable objects (see Ref.[68], for example). We can calculate the movement of deformable objects by expressing them as a network of mass points and springs and calculating spring forces between mass points. Spring-mass models have some advantages:

1. The modeling is intuitive.
2. Simulation can be easily carried out on personal work stations.
3. The model can represent various shapes of material.
4. It can represent fracture of objects by introducing breaking rule of springs.
5. Physical quantities in objects such as temperature distribution and stress distribution can be easily calculated.

From these advantages, we have adopted the numerical model based on the spring-mass model in this dissertation. As disadvanges of spring-mass models, in contrast, the models have a serious problem that the elastic force does not properly

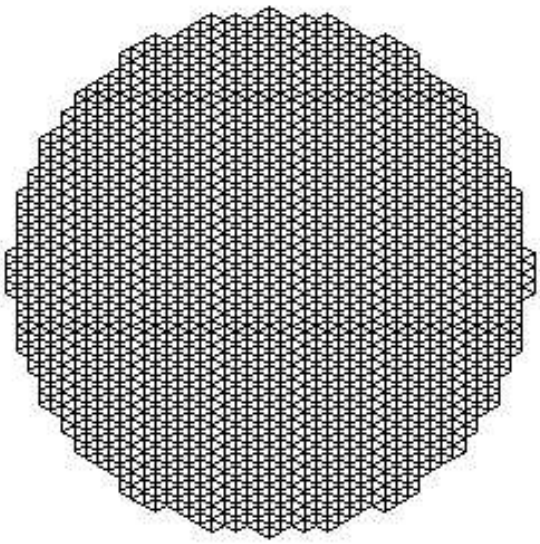

Figure 1.1: Schematic figure of triangular lattice model.

work for the restoration of deformation when configurations of two edge particles between a spring changed by large external forces. To avoid this effect, breaking rule of springs is sometimes introduced, which allows breaking of springs under extremely large applied forces [68, 69, 70]. In this dissertation, we do not introduce any breaking rule in our models. In chapter 2, we regard the state after such the problem occurs as plastic deformation. However, in this dissertation, most of simulations are carried out under the circumstances that deformation of models accurately restores.

Here, we introduce our numerical model based on the spring-mass model. We use some lattice geometries to represent elastic materials. In the next chapter, we use triangular lattice model to simulate the normal impact of a disk. In the triangular lattice disk(see Fig.1.1). All the mass points are connected with linear springs with spring constant κ. In the limit of a large number of mass points, this disk corresponds to the continuum circular disk with Young's modulus $E = 2\kappa/\sqrt{3}$ and Poisson's ratio $1/3$[71, 72]. As for the spring force, the position of

each mass point is governed by the following equation:

$$m\frac{d^2\mathbf{r}_i}{dt^2} = -\kappa\sum_{j=1}^{6}(d_0 - |\mathbf{r}_i - \mathbf{r}_j|)\frac{\mathbf{r}_i - \mathbf{r}_j}{|\mathbf{r}_i - \mathbf{r}_j|}, \tag{1.13}$$

where d_0 is the lattice constant, $\mathbf{r}_j$ is the position of the nearest neighbor mass points of $\mathbf{r}_i$, m is the mass of the mass points. Note that the directional projection of the linear spring force can cause the nonlinear deformation. By calculating forces acting each particle from springs and external force, we can calculate the positions of all particles in the next time step.

On the other hand, to simulate oblique impacts, we use random lattice to express elastic material instead of using regular lattice such as triangular lattice [39, 73, 74]. To make the random lattice disk, at first, we place mass particles in a circle with its radius R at the position $(x_i, y_i) = (r_i\cos\theta_i, r_i\sin\theta_i)$, where r_i and θ_i are uniform random numbers in the range of $0 \le r_i \le R$ and $0 \le \theta_i \le 2\pi$ respectively. After that, we connect all mass points with nonlinear springs using the Delaunay triangulation algorithm[75]. Figure 1.2 is the random lattice disk which is composed of 1099 mass points and 3153 springs. The spring interaction between connected mass points is described as

$$V_{ij}(x) = \frac{1}{2}k_a x_{ij}^2 + \frac{1}{4}k_b x_{ij}^4, \tag{1.14}$$

where x_{ij} is a stretch from the natural length of spring, and k_a and k_b are the spring constants. k_b is introduced to strengthen the model.

In this dissertation, we construct an elastic wall in addition to an elastic disk to simulate impacts between a disk and a wall. To construct the random lattice wall, similarly, we place mass points at the position (x_i, y_i), where x_i and y_i are uniform random numbers. The interaction between the disk and the wall during a collision is introduced as follows. Figure 1.3 is the schematic figure of the interaction between the disk and the wall. The right figure is the magnified figure in the circle on the left one. Total repulsion force of the disk is decided by a sum of the forces which are applied to mass points on the lower half boundary of the disk.

In our simulation, each mass point on the lower half boundary of the disk is reflected by the force

$$\mathbf{F}(l_s) = a_0 V_0 \exp(-a l_s)\mathbf{n}^s, \tag{1.15}$$

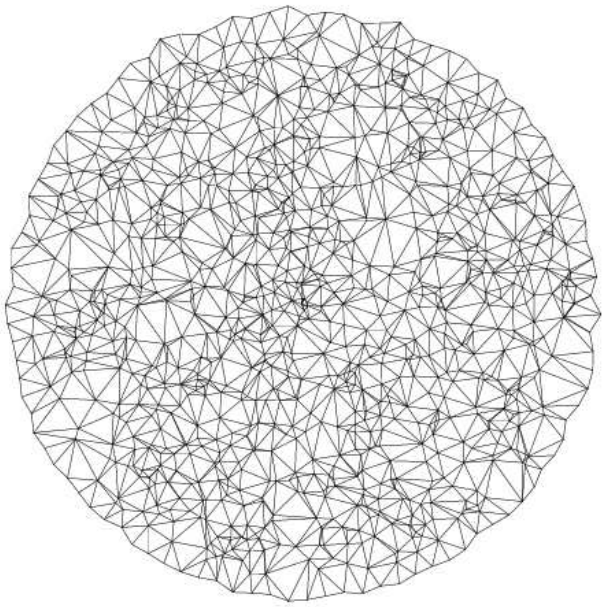

Figure 1.2: The random lattice disk with rough surface.

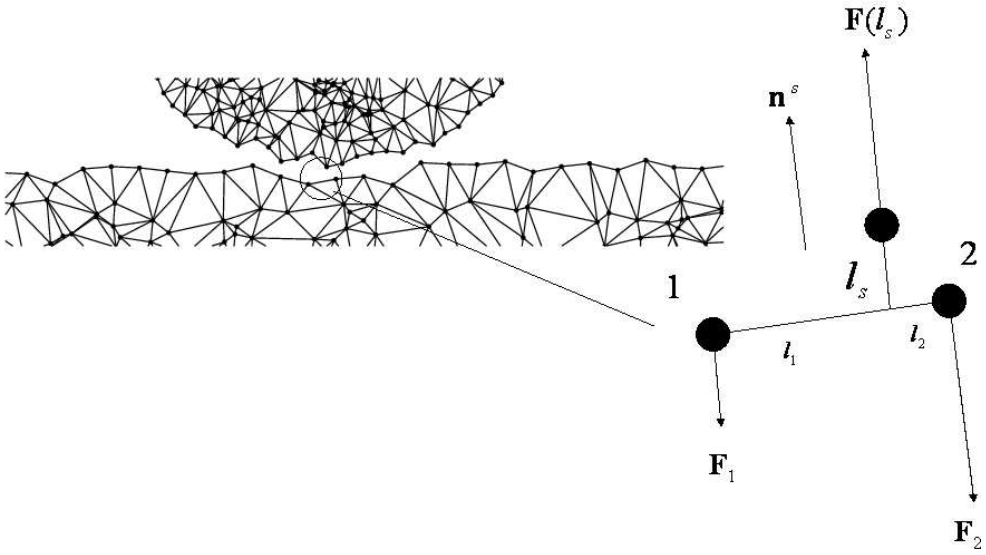

Figure 1.3: Interaction between surface particles of the disk and the wall.

where $a_0 = 300/R$, $V_0 = amc^2R/2$, l_s is the distance between each surface mass point of the disk and its nearest surface spring of the wall, and $\mathbf{n}^s$ is the normal unit vector to the spring. We adopted an exponential function as a strong repulsion force to inhibit penetrations of mass points of the disk to springs of the wall surface. The exponential function may be replaced by a strong repulsion among atoms like $\sim l_s^{-12}$ coming from Lennard-Jones potential. However we have adopted a single exponential function following the idea in Ref.[37] [2]. Two mass points 1 and 2 of both ends of the spring are respectively applied by the reaction force, $\mathbf{F}_1(l_s) = -\frac{\mathbf{F}(l_s)}{1+l_1/l_2}\mathbf{n}^s$ and $\mathbf{F}_2(l_s) = -\frac{\mathbf{F}(l_s)}{1+l_2/l_1}\mathbf{n}^s$, which are decided by the balance of the torques. Thus, the equation of motion for each mass point

[2]The properties of force laws among two granular particles used in simulations were systematically investigated by Schäfer *et al.* [76].

on the lower half boundary of the disk is represented by

$$m\frac{d^2\mathbf{r}_i}{dt^2} = \sum_{j=1}^{N_i}\left\{-k_a\mathbf{x}_{ij} - k_b\mathbf{x}_{ij}^3\right\} + \theta(l_s - l_{th})a_0V_0\exp(-a_0l_s), \tag{1.16}$$

where m is mass, $\mathbf{r}_i$ is the position of i-th mass point, $\mathbf{x}_{ij}$ is a stretch between i-th particle and j-th particle from the natural length, N_i is the number of mass points connected to i-th mass point, and $\theta(l_s - l_{th})$ is a step function which is defined by

$$\theta(l_s - l_{th}) = \begin{cases} 1 & \text{if } l_s \leq l_{th} \\ 0 & \text{if } l_s > l_{th}, \end{cases}$$

where l_{th} is a threshold which is the average of natural lengths of all springs of the disk. For other mass points, the last term of the right hand side of Eq.(1.16) is omitted. The sum of Eq.(1.16) for all i-th mass points corresponds to the repulsion force applied to the disk.

In the simulation of oblique impacts with the random lattice model, roughness of the surfaces is important to make the disk rotate after collisions. To make roughness, at first, we generate normal random numbers whose average value is 0 and then make the initial position of particles on surfaces of both the disk and the wall deviate with them. In most of our simulation in this dissertation, we choose the standard deviation of the normal random numbers δ as $\delta = 3 \times 10^{-2}R$, where R is the radius of the disk.

In the random lattice model, we measure elastic constants such as Young's modulus E and Poisson's ratio ν by stretching mechanically a band of random lattice and measuring strains in vertical and horizontal directions. Details about measuring them are treated in chapter 4.

1.4 The composition of the dissertation

Here, we present brief outlines of each chapter of the dissertation. In chapter 2, the normal impact of an elastic disk to a potential wall will be demonstrated by simulation as in experiment. We reproduce that COR decreases with increasing impact velocity. In chapter 3, the normal impact of an elastic disk to an elastic wall will be demonstrated by simulation. We will show that COR depends on the thickness of the wall which is similar to the experimental results by Sondergaard *et al.*. In chapter 4, the oblique impact between an elastic disk and an elastic wall will be demonstrated by simulation. Our numerical results of the relation

between coefficient of tangential restitution and incident angle can be well reproduced by Maw's theory of oblique impacts[27, 28]. In chapter 5, the oblique impact between a hard elastic disk and a soft elastic wall, which corresponds to the experiment by Louge and Adams[30], will be demonstrated by simulation and analyzed theoretically. Chapters 6 and 7 are devoted to the general discussion and conclusion of the dissertation.

Appendices A and B are devoted to derivations of Walton's simple argument and Maw's theory of oblique impacts, respectively. In Appendix C, we explain the calculation of Young's modulus and Poisson's ratio of a square lattice system. In Appendix D, the contact problem of a hard disk on an elasic half-space is theoretically treated. Appendix E is a simple chronological table of impact studies.

Chapter 2

Normal impact of an elastic disk on a wall without internal structure

In this chapter, we demonstrate impacts of two-dimensional elastic disks with a potential wall numerically. We introduce two simulation methods: one is based on a lattice model (model A) and another is based on a continuum model (model B) which is identical to that by Gerl and Zippelius[37]. Both models do not include any dissipation. Thus, we assume that inelastic collisions take place only from the transfer of modes of oscillation. Through our simulation, we will demonstrate that the elastic models do not recover the results predicted by the quasi-static theories in the low impact velocity [26, 33, 34, 35, 36].

2.1 Models

Let us explain details of our models to simulate collisions between two identical disks with radius R by the method of the mirror image. Here, we carry out impact simulation with two kinds of numerical models: model A and model B. In both models, the wall exists at $y = 0$, and the center of mass of the disk keeps the position at $x = 0$. The disk approaches from the region $y > 0$ before rebounding from the wall (see Fig.2.1).

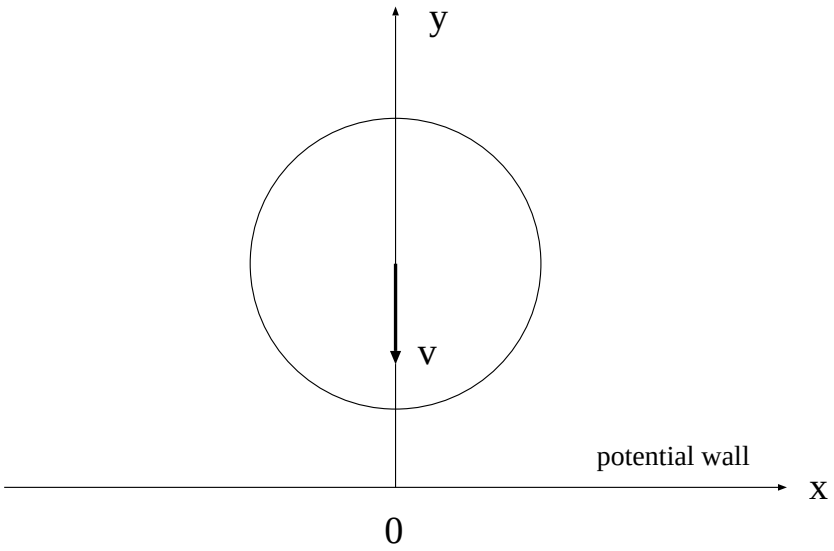

Figure 2.1: The disk of model A or B approaching to the potential wall.

2.1.1 Model A

Model A consists of 1459 mass points (with the mass m) on a triangular lattice. The position of each mass point of model A is governed by the following equation:

$$m\frac{d^2\mathbf{r}_i}{dt^2} = -\kappa\sum_{j=1}^{6}(d_0 - |\mathbf{r}_i - \mathbf{r}_j|)\frac{\mathbf{r}_i - \mathbf{r}_j}{|\mathbf{r}_i - \mathbf{r}_j|} + \mathbf{n}a_0V_0e^{-a_0y_i}, \tag{2.1}$$

where d_0 is the lattice constant, $\mathbf{r}_j$ is the position of the nearest neighbor mass points of $\mathbf{r}_i$, m is the mass of the mass points, y_i is the y coordinate of $\mathbf{r}_i$, and $\mathbf{n}$ is the unit vector in the y direction. The wall potential is given by $V_0e^{-a_0y}$, where $V_0 = mc^2a_0d_0/2$ with $c = \sqrt{E/\rho}$ and the density ρ. We adopt $a_0 = 100/d_0$ for the most of simulations, but we also adopt the result of $a_0 = 25/d_0 = 500/R$ to obtain Fig. 2.2, though the result is almost identical to that for $a = 100/d_0$. The exponential interaction between the disk and the wall is introduced to simulate a collision between two identical disks. Actually, in the limit of $a_0 \to \infty$, the exponential potential can be regarded as a potential of the mirror image. Thus, for later calculation, we analyze the case for large a_0d_0. The convergence of the result on the number of mass points are roughly checked in this model.

2.1.2 Model B

In this subsection, we introduce model B which is originally proposed by Gerl and Zippelius[37]. Although the details of this model can be found in their paper, we present a short description of this model to understand the setup of our simulation.

Gerl and Zippelius[37] analyze Hamilton's equation to simulate collisions of a disk with the radius R as;

$$\dot{P}_{n,l} = -\frac{\partial H}{\partial Q_{n,l}}; \quad \dot{Q}_{n,l} = \frac{\partial H}{\partial P_{n,l}} \tag{2.2}$$

under the Hamiltonian

$$H = \frac{P_0^2}{2M} + \sum_{n,l}^{N}(\frac{P_{n,l}^2}{2M} + \frac{1}{2}M\omega_{n,l}^2 Q_{n,l}^2) + V_1 \int_{-\pi/2}^{\pi/2} d\phi e^{-a_0 y(\phi,t)}. \tag{2.3}$$

Here M is the (two-dimensional) mass of an elastic disk, and $Q_{n,l}$ is the expansion coefficient of the 2D elastic deformation field in the polar coordinate $\mathbf{u} = (u_r, u_\phi)$,

$$(u_r(r,\phi), u_\phi(r,\phi)) = \sum_{n,l} Q_{n,l}(u_r^{n,l}(r)\cos n\phi, u_\phi^{n,l}(r)\sin n\phi), \tag{2.4}$$

where $u_r^{n,l}(r)R = A_{n,l}\frac{dJ_n(k_{n,l}r)}{dr} + nB_{n,l}\frac{J_n(k'_{n,l}r)}{r}$ and $u_\phi^{n,l}(r)R = -nA_{n,l}\frac{J_n(k'_{n,l}r)}{r} - B_{n,l}\frac{dJ_{n,l}(k_{n,l}r)}{dr}$ with the radius of the disk and the Bessel function of the $n-$th order $J_n(x)$. Here $k'_{n,l} = k_{n,l}\sqrt{2(1+\nu)/(1-\nu^2)}$, and $k_{n,l}$ is the solution of

$$\begin{aligned}&(1-\nu^2)(1-n^2)\kappa\kappa^{'2}J_{n-1}(\kappa)J_{n-1}(\kappa^{'}) + \kappa^2[\kappa^2 - 2n(n+1)(1-\nu)]J_n(\kappa)J_n(\kappa^{'}) \\ &+(1-\nu)[\kappa^2 - (1-\nu)(1-n^2)n][\kappa J_{n-1}(\kappa)J_n(\kappa^{'}) + \kappa^{'}J_{n-1}(\kappa^{'})J_n(\kappa)] = 0\end{aligned} \tag{2.5}$$

with Poisson's ratio ν, $\kappa = k_{n,l}R$ and $\kappa^{'} = k'_{n,l}R$, which is given by the force free boundary condition of the disk. Thus, for fixed n there are infinitely many solutions $k_{n,l}$ and $\omega_{n,l} = k_{n,l}\sqrt{E/\{\rho(1-\nu^2)\}}$ numbered by $l = 0, 1, \cdots, \infty$. $A_{n,l}$ and $B_{n,l}$ are determined by

$$\begin{aligned}&-A_n[\frac{(1-\nu)}{R}\frac{dJ_n(k_{n,l}R)}{dR} + (k_{n,l}^2 - \frac{(1-\nu)}{R^2}n^2)J_n(k_{n,l}R)] \\ &+nB_n(1-\nu)[\frac{1}{R}\frac{dJ_n(k'_{n,l}R)}{dR} - \frac{J_n(k'_{n,l}R)}{R^2}] = 0\end{aligned} \tag{2.6}$$

and $\int_0^R drr\{{u_r^{n,l}}^2 + {u_\phi^{n,l}}^2\} = R^2$. $P_{n,l}$ is the canonical momentum. $y(\phi, t)$ is the shape of the elastic disk in polar coordinates;

$$y(\phi, t) = y_0(t) + \sum_{n,l} Q_{n,l}(C_{n,l}\cos(n\phi)\cos\phi - S_{n,l}\sin(n\phi)\sin\phi) \qquad (2.7)$$

with the position of the center of mass $y_0(t)$ and constants $C_{n,l}$ and $S_{n,l}$ determined by the maximal radial and tangential displacement at the edge of the disk as $C_{n,l} = u_r^{n,l}(R)$ and $S_{n,l} = u_\phi^{n,l}(R)$. M is the mass of the disk, and the momentum of the center of the mass $P_0 = M\dot{y_0}$ satisfies $\dot{P}_0 = -(\partial H/\partial y_0)$, V_0 and a are parameters to express the strength of the wall potential.

For the simulation of a pair of identical disks, they have confirmed that the result with finite a_0 can be extrapolated to the result of $a_0 \to \infty$ by taking into account finite a_0 effect in proportion to $1/(a_0 R)$. Similarly, the result with finite number of modes N should be extrapolated with the correction in proportion to $1/\sqrt{N}$. Since they have already checked such the tendencies, we only adopt $N = 1189$ ($n \leq 50$) or $N = 437$ ($n \leq 30$), $V_1 = Mc^2 aR/2$, and $a_0 = 500/R$.

2.1.3 Parameters in both models

For the comparison between two different models, we only simulate the case of Poisson's ratio $\nu = 1/3$. The numerical integration scheme for model A is the classical fourth order Runge-Kutta method with $\Delta t = 1.6 \times 10^{-3}\sqrt{m/\kappa}$. Parts of the calculation in model A has been checked by the fourth order symplectic integral method with $\Delta t = 5.0 \times 10^{-3}\sqrt{m/\kappa}$, and no differences in results of two methods can be found. For model B, we adopt the fourth order symplectic integral method with $\Delta t = 5.0 \times 10^{-3} R/c$. In both models, we have checked for conservation of the total energy.

We also investigate the impact with finite temperature. The temperature is introduced as follows: In model A, we prepare the Maxwellian for the initial velocity distribution of mass points, where the positions of all mass points are located at their equilibrium positions. From the variance of the Maxwellian we can introduce the temperature as a parameter. To perform the simulation, we prepare 10 independent samples obeying Maxwellian with the aid of normal random number. In model B, we prepare samples which satisfy Gibbs states. Namely, $\sqrt{M}\omega_{n,l}Q_{n,l}/\sqrt{2}$ and $P_{n,l}/\sqrt{2M}$ obey the normal random number with the variance (temperature) T. In model B, we prepare many samples (120 or 20) to simulate systems at finite T.

The summary of differences between model A and B is as follows: (i) All of the mass points in model A interact with the wall. However, in model B, only the exterior boundary has the influence of the potential as in Eq.(2.3). We have replaced the original model A by a model in which only mass points on the boundary can interact with the wall. However we cannot find significant differences in the results of our simulation in both discrete models. (ii) Model A can have nonlinear deformations, but model B is based on the theory of linear elasticity. (iii) Model A can express some plastic deformations while model B cannot. This effect will be discussed later. (iv) Model A has six fold symmetry while model B has only rotational symmetry. (v) The force free boundary condition is assumed in model B though it may not be appropriate for actual situations. Model A does not include such the condition.

2.2 Results

Now, let us explain the details of our simulation. We will introduce the results at $T = 0$ and at finite T by turns.

2.2.1 Simulation at $T = 0$

At first, we carry out the simulation of model A and model B with the initial condition at $T = 0$ (*i.e.* no internal motion). Figure 2.2 is the plot of the COR against the impact velocity for both model A and model B. For model A, we have adopted the fourth order Runge-Kutta method. To eliminate the effect of six fold symmetry of model A, we average 12 data as a function θ of the initial orientations of the disk i.e. $\theta = \pi n/72$ with $n = 1, 2, 3, \cdots, 12$ with $a_0 = 25/d_0 = 500/R$. We also investigate the case that only mass points at the boundary can interact with the wall for small v_i but their results do not have any visible difference from the original model A. It is obvious that there is no plastic deformations for $v_i \leq 0.2c$.

For model B, we show the results of 437 modes and 1189 modes which clearly demonstrates the convergence of the result for the number of modes. When impact velocity v_i is larger than $0.1c$ with $c = \sqrt{E/\rho}$, the value of COR of model A is almost identical to that of model B. Each line decreases smoothly with increasing impact velocity.

At present, we do not know the reason why the significant difference between the two models exists at low impact velocity. It is difficult to imagine that occur-

rence of nonlinear deformations during the impact of model A causes the difference because the deformation is smaller when v_i is smaller.

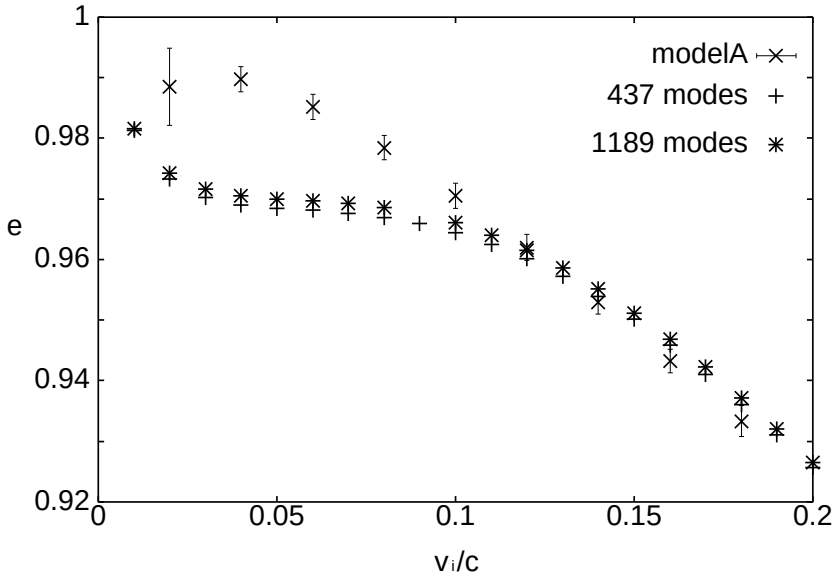

Figure 2.2: Coefficient of restitution for normal collision of the Model A and Model B as a function of impact velocity, where $c = \sqrt{E/\rho}$ with the Young's modulus E and the density ρ. 437 and 1189 modes are chosen for model B.

Second, we investigate the force acting on the center of mass of the disk caused by the interaction with the wall in model B. In the limit of $v_i \to 0$ we expect that the Hertzian contact theory can be used[49, 25, 37]. The small amount of energy transfer from the translational motion to the internal motion is the macroscopic dissipation. Thus, we can check whether the quasi-static approaches [26, 33, 34] or our elastic simulation can be used in slow impact situations.

If h is given, we can calculate the elastic force by solving Eq.(1.7) numerically. Figure 3 is the comparison with our simulation in model B (1189 modes) and the Hertzian contact theory Eq.(1.7) which is given by the solid lines. The result of our simulation at the impact velocity $v_i = 0.01c$ shows the hysteresis as suggested in the simulation at $v_i = 0.1c$[37]. This means the compression and rebound are not symmetric. The hysteresis curve is still self-similar even at $v_i = 0.04c$ but the loop becomes noisy at $v_i = 0.1c$.

For very low impact velocity $v_i = 0.001c$, the hysteresis loop almost disap-

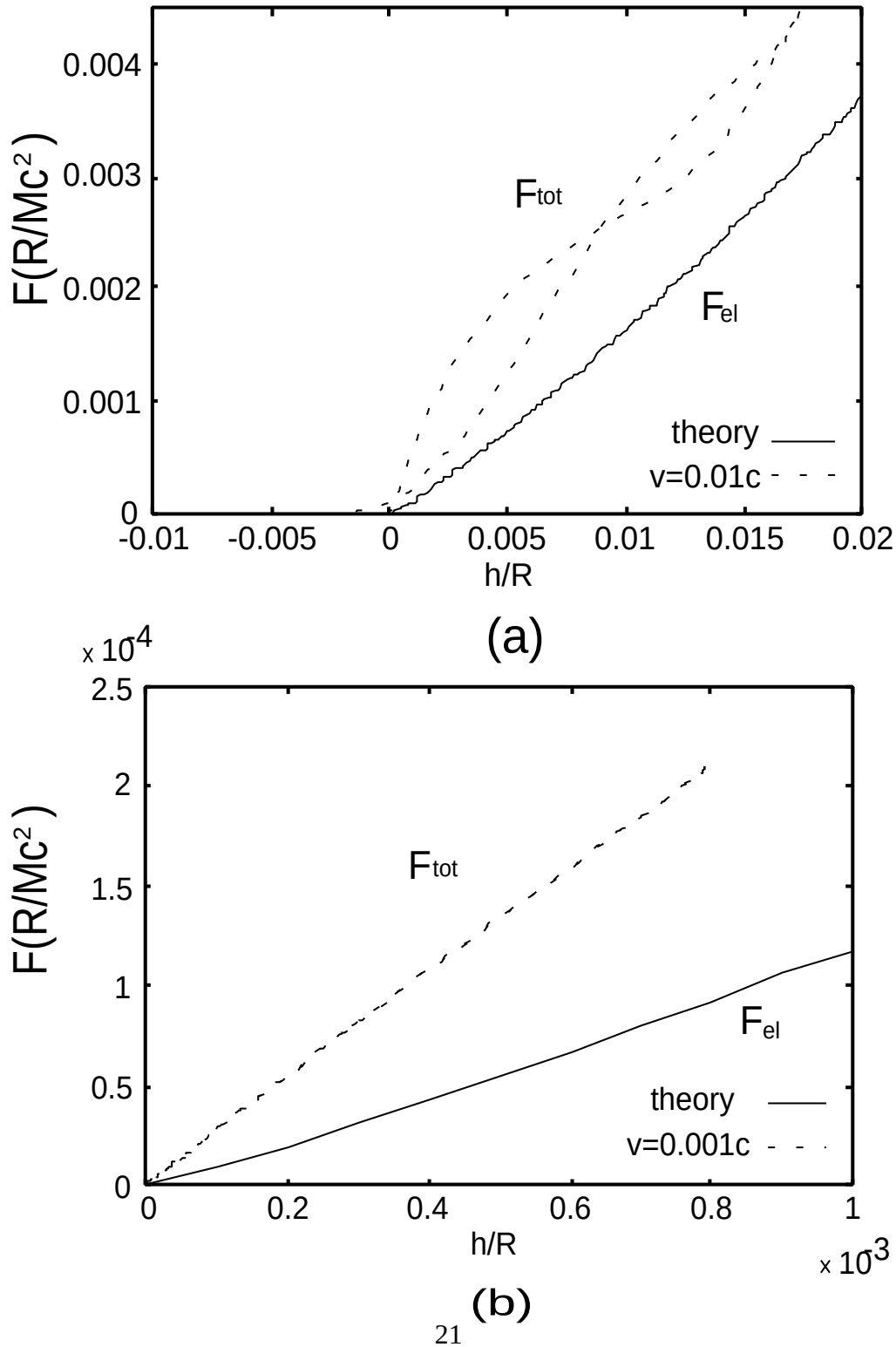

Figure 2.3: The comparison of the Hertzian force in Eq.(1.7) with our simulation at $v_i = 0.01c$ (a) and $v_i = 0.001c$(b) at $T = 0$ in model B. F_{tot} is the total force originated from the interaction with a wall.

pears and the total force observed in our simulation is almost a linear function of h which deviates from the one predicted by both the Hertzian contact theory and the quasi-static theory (Eq.(1.10)). In particular, the turning point which corresponds to the point of the largest F_{tot} in Fig. 2.3(b) is apart from the Hertzian curve (the solid line). This deviation is in clear contrast to the quasi-static theory, because the dissipative force in the theory in Eq.(1.10) must be zero at the turning point which $dh/dt = 0$ should satisfy. This tendency is invariant even for the simulation of model A, though the data become noisy. The linearity of the total repulsion force is not surprising, because $e^{-a_0 y(\phi,t)}$ in the potential term in Eq.(2.3) can be expanded in a series of $Q_{n,l}$ for very slow impact.

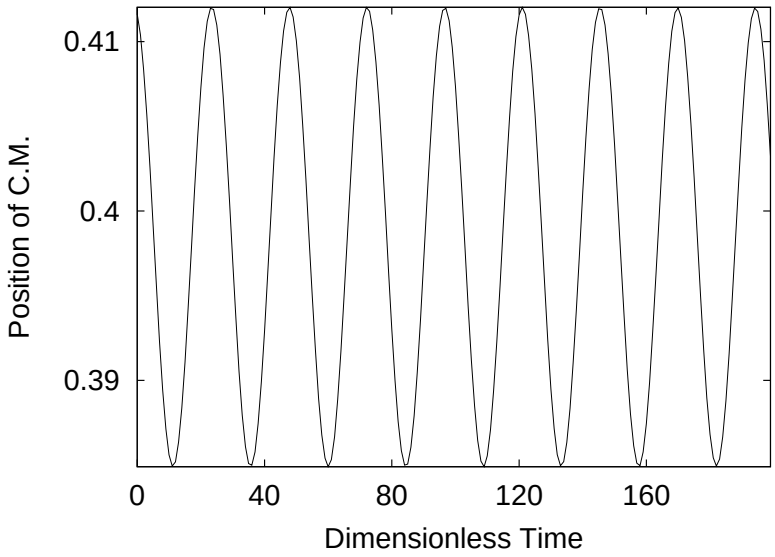

Figure 2.4: The time evolution of the center of mass of the elastic disk under the compression by $g = 0.01c^2/R$ (model B with N=437). Here the dimensionless time is measured by R/c and the position of C.M. (center of mass) is measured by the diameter of the disk (2R). Simulation is performed at the finite temperature $T = 10^{-8}Mc^2$ and is averaged over 20 independent samples which start from initial condition satisfying the Gibbs distribution.

The result may suggest that our elastic models do not recover the Hertzian contact theory in the quasi-static limit. To check the tendency, we investigate whether any static state can be achieved in our models in the compression. Figure

2.4 is the time evolution of the center of mass in the simulation of model B, where the strength of dimensionless external field is $g = 0.01c^2/R$. We observe that an undamped harmonic oscillation of the center of mass in the simulation after the first deformation. This oscillation is stable because the energy of oscillation is not enough to overcome finite energy gap between energy levels. Thus, the center of mass keeps the oscillation as the motion in the ground state. We note that Fig.2.4 is the result of the simulation at finite temperature in which the mode transfer is enhanced. Nevertheless, the center of mass keeps the harmonic oscillation. This tendency can be observed in model A, too. Even when we introduce the randomness in the coupling in model A, the oscillation is undamped. Thus, both of elastic models cannot reach any equilibrium steady state as is assumed in the Hertzian contact theory. This result indicates that the elastic models are not appropriate to describe quasi-static situations for $v_i/c \ll 1$. Note that the introduction of nonlinear deformation may not be enough, because as we can see in Fig. 2.3 (b) the deformation is very small for slow impact. Thus, it is difficult to imagine the impact produces nonlinear deformations. To reach an equilibrium state, thus, we need to introduce some microscopic dissipative mechanism.

However, the validity of the contact time t_f in the impact evaluated as $t_f \simeq (\pi R/c)\sqrt{\ln(4c/v_i)}$ by the quasi-static theory[37] has been confirmed by the results of our simulation of model A (Fig. 2.5). Thus, our elastic model can be valid in the impact with the intermediate speed.

2.2.2 Simulation at finite T

Now, let us show the results of our simulation at finite T. The thermal velocity $v_{th} = \sqrt{T/M}$ causes significant differences from those at $T = 0$ in both low and large impact velocities. In this sense, we have much room to study this process at finite T systematically.

For small impact velocity, i.e. if the effect of v_{th} is not negligible, the fluctuation of COR at finite T becomes large, while the average is almost independent of temperature as in Figs. 2.6 and 2.7, where the results are obtained from the average of 120 independent samples. In some trials at high temperature, thus, COR becomes larger than 1, though the average is less than 1. Of course, for such the high temperature, it is impossible to control the actual speed of impact.

For large impact velocity, $v_i \gg v_{th}$, we do not observe any definite temperature effect in model B but we find drastic decrease of COR in model A. It seems that COR can be on a universal curve when the impact velocity is scaled by the

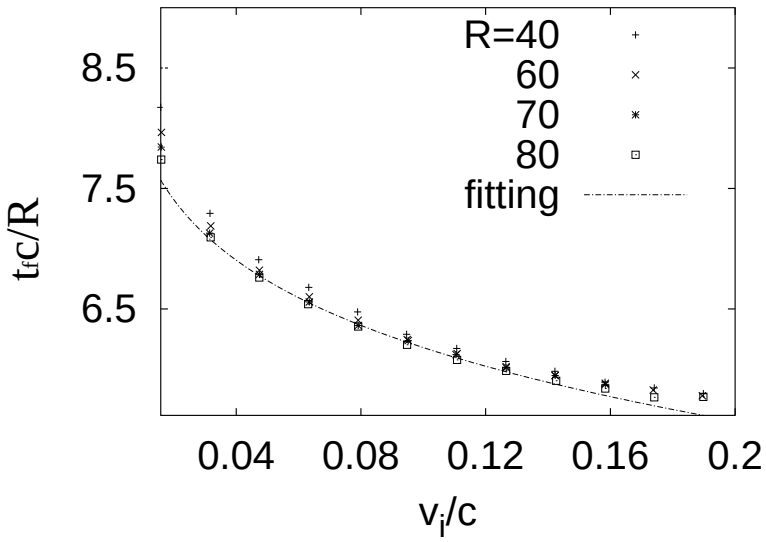

Figure 2.5: The plot of contact time versus the impact velocity. R represents the radius of the disk, in which $R = 40$,60,70 and 80 correspond to the number of mass points 5815, 13057, 17761 and 23233, respectively. The dotted line is fitting curve based on the quasi-static theory.

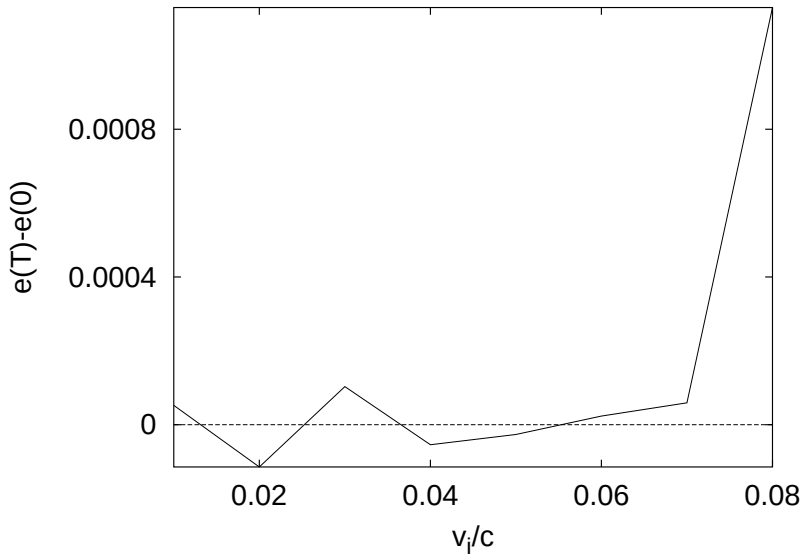

Figure 2.6: The average shift of COR at finite temperature $T = 10^{-8}Mc^2$ as a function of the impact velocity in model B with $N = 437$.

critical velocity above which the COR decreases abruptly (Fig. 2.8). The relation between the critical velocity and the initial temperature at the intermediate impact velocities is shown in Fig. 2.9. The critical velocity seems to obey a linear function of T, though the data is not on the function for both slow and fast impacts.

2.3 Discussion

We investigate what happens in the disk above the critical velocity and find the existence of plastic deformation of the disk (Fig. 2.10(a)). Actually, there are no energy differences between two configurations in Fig. 2.10(b) which can occur after the strong compression during the impact but cannot be released after the impact is over. It is well known that plastic deformation causes the drop of the COR[25].

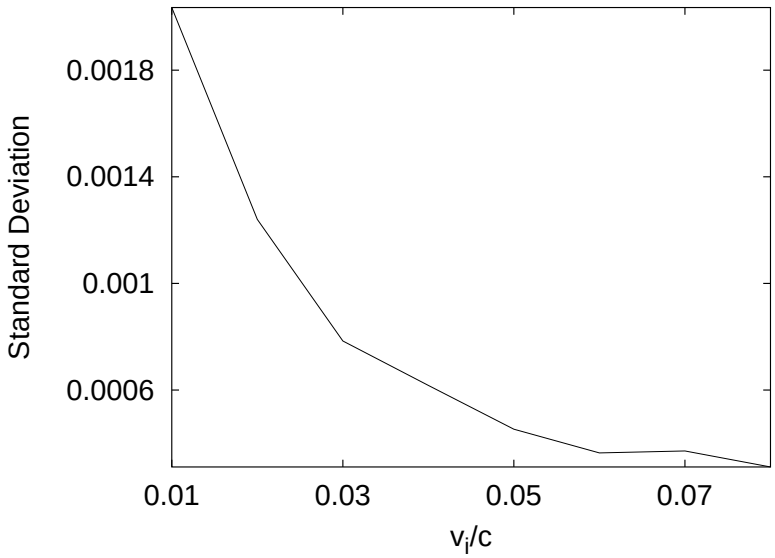

Figure 2.7: The standard deviation of COR $\sqrt{(e- < e >)^2}$ at $T = 10^{-8}Mc^2$ as a function of the impact velocity v_i via model B with $N = 437$.

2.3.1 Application of the conventional theory of plastic deformation to 2D impacts

Following the description by Johnson[25], let us explain the dimensional analysis of the two-dimensional plastic deformation. From two-dimensional Hertzian law Eq.(1.7) we evaluate $h \sim a^2/R$[25]. The work for the compression of the disk W is $W = (1/2)Mv_i^2 \sim \int_0^{h^*} dhF_{el} \sim \int_0^{a^*} daa^3/R^2$, where M and v_i are the mass of the disk and the impact velocity, respectively. h^* and a^* are respectively the maximal compression and and the maximal contact length. Here we neglect the logarithmic correction and unimportant numerical factors. Introducing the mean contact pressure during dynamical loading p_d which satisfies $p_d \sim F_{el}/a$, W can be evaluated by $W \sim F_{el}h^* \sim p_d(a^*)^3/R$. From $W \sim Mv_i^2$ we can express $a^* \sim (Mv_i^2R/p_d)^{1/3}$.

Let us assume that the impact exceeds the yield pressure for the plastic deformation. In such the case, the deformation does not restore correctly after rebound. Thus, the work in a rebound is $W' \sim F^*h^*$ where F^* is the maximal force during the impact. From $h^* \sim F^*/E$ and $F^* \sim p_da^*$ we evaluate $W' \sim (p_da^*)^2/E$.

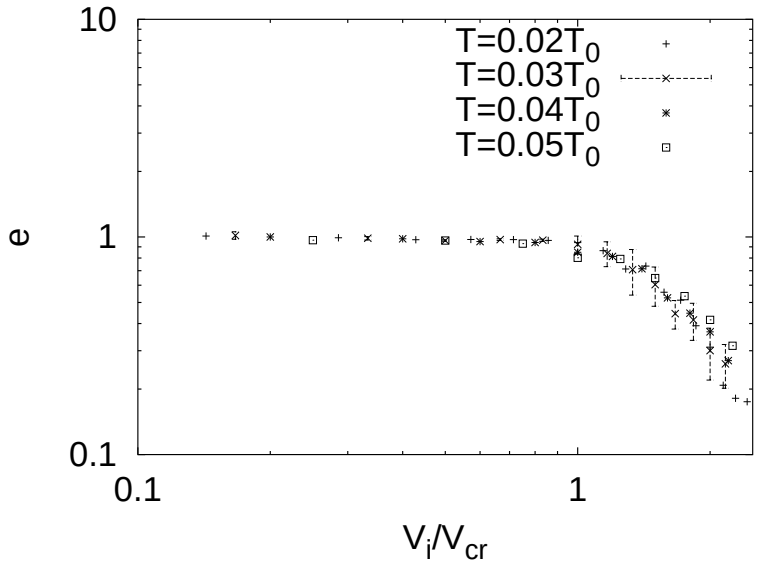

Figure 2.8: The relation the coefficient of restitution and the impact velocity rescaled by the critical velocity for each temperature. Curves are plotted in the log-log scale. The temperature is scaled by $T_0 = mc^2$ with the mass of the mass points m. Note that the error bars are plotted only in the case $T/T_0 = 0.03$ but is the same order even at other T (model A).

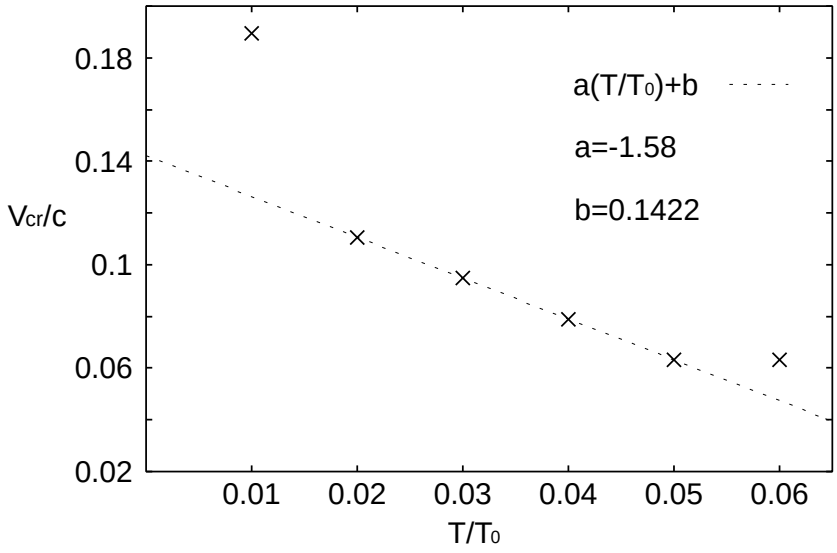

Figure 2.9: The plot of the initial temperature and the critical velocity causing the plastic deformation. $v_{cr}/c = a(T/T_0) + b$ is the fitting curve line from the data between $T/T_0 = 0.02$ and 0.05 (model A).

(a)

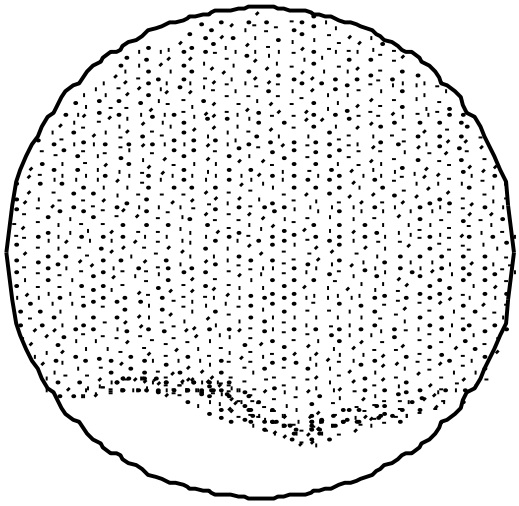

(b)

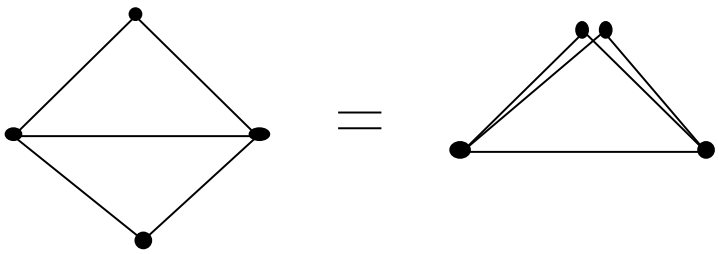

Figure 2.10: (a) Plastic deformation of model A with $v_i = 0.22c$ at $T = 0.03mc^2$. The solid line represents the initial circle. The points in a circle are positions of the mass points after the collision. The deformation is asymmetric because of the velocity distribution at the initial stage. (b) All the mass points of the disk initially consist of triangular lattice. When the deformation occurs, it is possible that the configurations of mass points (points in figure) locally change like this figure. Note that these two configurations are energetically equivalent.

Substituting the expression of a^* into the expression for W and W' we obtain the COR as

$$e^2 = \frac{v_r^2}{v_i^2} = \frac{W'}{W} \sim \frac{p_d^{4/3} R^{2/3}}{E(M v_i^2)^{1/3}}. \tag{2.8}$$

Thus, we expect the law $e \sim v_i^{-1/3}$ in the collision of a plastic deformed disk. The three dimensional version of evaluation which gives $e \sim v_i^{-1/4}$ agrees well with the experiment[25].

2.3.2 Realistic systems

The actual plastic deformation is more complicated than what we modeled in this paper. For example, in the actual contact area a central region of perfect contact is surrounded by an annulus of imperfect contact. In actual situations, it is not easy to obtain a pure normal collision, because the rotation of disks is difficult to be suppressed and the wall is not perfectly flat. Thus, a little deviation of the collision angle causes the tangential stress in collisions. In the existence of tangential stress, we need to consider the effect of imperfect contact or partial slip in the outer region to get finite force at the corner of contact area.

We also note that the actual materials are not uniform. They contain a lot of microcracks, and amorphous structure locally. Such the imperfection of the materials causes the local achievement of the yield of plastic deformation. Thus, the plastic deformation also occurs locally in contrast to the macroscopic deformation in Fig.2.10.

Our finding is, however, something new, because (i) the decrease of COR is excited by the temperature and (ii) COR decreases more rapidly like $e \sim v_i^{-1.2}$ than that for the conventional plastic deformation $e \sim v_i^{-1/3}$ in Eq. (2.8). The mechanism how to occur the plastic deformation is not clear at present including the linear law in Fig. 2.9.

For future refinement of our model to describe plastic deformation, we need to introduce (i) the initial cracks, (ii) local deformation of lattices at the initial condition, (iii) the yield of local plastic deformation or non-Hookian effects of springs, and (iv) porosity distribution at the initial condition. Of course, to compare the simulation with experiments, we have to simulate the model in three dimensional situations.

2.4 Conclusion of this chapter

We have numerically studied the impact of a two-dimensional elastic disk with a potential wall with the aid of model A and model B. The result can be summarized as (i) The coefficient of restitution (COR) decreases with the impact velocity. (ii) The result of our simulation is not consistent with the result of the two-dimensional quasi-static theory. For large impact velocity, there is hysteresis in the deformation of the center of mass. For small velocity, there remains the inelastic force even at $dh/dt = 0$. (iii) The effect of heat diffusion may be important for the small impact velocity. (iv) There are drastic effects of temperature in both small and large impact velocity. (v) In particular, for large impact velocity of model A, we have found the abrupt drop of COR above the critical impact velocity by the plastic deformation. The critical velocity of the plastic deformation seems to obey a simple linear function of temperature.

Chapter 3

The coefficient of restitution as a function of wall thickness

In this chapter, the impact of an elastic disk with an elastic wall is numerically studied. We introduce a numerical model of an elastic disk and an elastic wall by mass points and linear springs. From our simulation, we confirm that the coefficient of normal restitution depends on the thickness of the elastic wall.

3.1 Introduction

In the previous chapter, we introduced two different numerical models to investigate impact of an elastic disk with a structureless wall[38, 39]. One of them is the lattice model consisted of mass particles and linear springs. Another is the continuum model which is identical to that by Gerl and Zippelius[37]. With these two models, we investigated the relation between the impact velocity and the coefficient of normal restitution, etc[38, 39]. These two models have common features in that (i) they have no dissipative mechanism and (ii) the wall has no internal degrees of freedom. In actual situations of collision between a disk and a wall, however, a part of initial energy of the disk is transfered into the wall. Thus, we have to introduce internal degrees of freedom of the wall to simulate impacts between the disk and the wall. As for the normal impact between a metal sphere and a wall, Sondergaard *et al.* demonstrated that the coefficient of restitution depends on the thickness of the wall[15]. Their experimental results are well reproduced by the theory of plate response under point force by Zener[77].

In this chapter, we perform simulations of the normal impact of an elastic disk

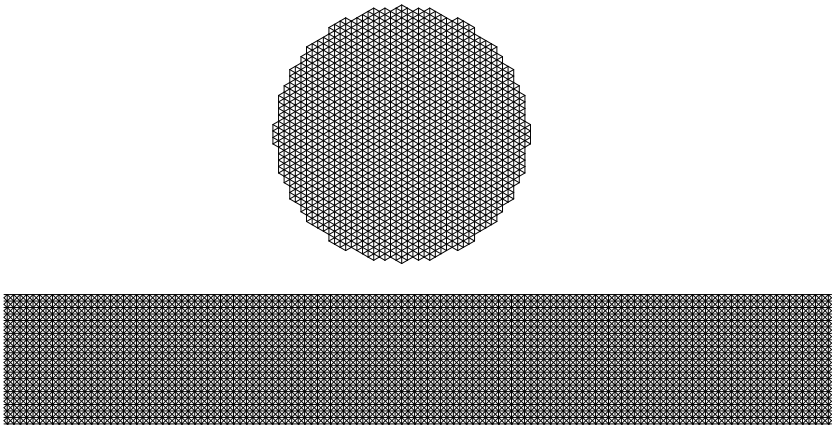

Figure 3.1: Impact model consisted from an elastic disk and an elastic wall.

with an elastic wall. In the next section, we will introduce our two-dimensional model consisted of an elastic disk and an elastic wall. In section 3.3, we will show the result of our simulation. The final section is devoted to the conclusion remarks of this chapter.

3.2 Model

Let us introduce our numerical model. We adopt the triangular lattice model of 1459 mass points as an elastic disk(see Fig.3.1). We also introduce the elastic wall of 6400 mass points on a square lattice. We introduce two spring constants for spring interactions of the wall: k_1 for nearest neighbor interaction and k_2 for next-nearest neighbor interaction for the wall. Controlling k_1 and k_2, we can change the material constant of the elastic wall[69, 70] (see appendix C). We set k_1 and k_2 as Young's modulus of the elastic wall is equal to that of the elastic

disk when the force is applied to the wall in the normal direction. The width of the wall is 4 times as long as the diameter of the disk. Two sides of the wall are fixed. We can choose any thickness of the wall. As for the interaction between the disk and the wall during a collision, we adopt $a_0 = 100/d_0$ for the repulsive force of the disk. To perform the numerical simulation, we scale all parameters by the radius of the disk R and the speed of sound $c = \sqrt{E/\rho}$, where ρ is the density of the disk. We adopted the fourth order symplectic numerical method with the time step $\Delta t = 10^{-2}R/c$ (R is the radius of the disk) as the numerical scheme of integration.

3.3 Simulation result

Sondergaard *et al.* investigated the influence of the ratio of the diameter of sphere to the plate thickness on the coefficient of restitution resulting in normal impacts[15]. They dropped ball bearings(steel or bronze) and glass spheres without any significant rotational velocity from various heights onto plates of lucite or aluminum of which two sides were solidly clamped to a relatively rigid support structure. From their experiment, the coefficient of restitution decreases as the ratio of the particle diameter to the plate thickness increase.

We set our situation corresponding to the experiment by Sondergaard *et. al.*[15] to carry out our simulation of the normal impact. Our situation is as follows. We control the ratio of the disk diameter D_d to the wall thickness T_w, D_d/T_w, from 0.4 to 1.0. We make the disk collide against the wall with various initial velocity ranging from $0.02c$ to $0.18c$ and calculate the coefficient of restitution (Fig. 3.2). When the impact velocity has same value, the coefficient of restitution of small D_d/T_w is larger than that of large D_d/T_w. The curve labeled model A is the result of the case that the lattice model of the disk and the wall with no internal degrees of freedom[39].

3.4 Conclusion remarks

We have performed the normal impact of the elastic disk with the wall. In the case of the normal impact, the coefficient of restitution e depends on the ratio of the diameter of the disk to the thickness of the wall D_d/T_w. If D_d/T_w is large, e is small. It is seen that the macroscopic vibration of the wall is so large that initial energy of the disk decreases. Sondergaard *et al.* introduced the impact

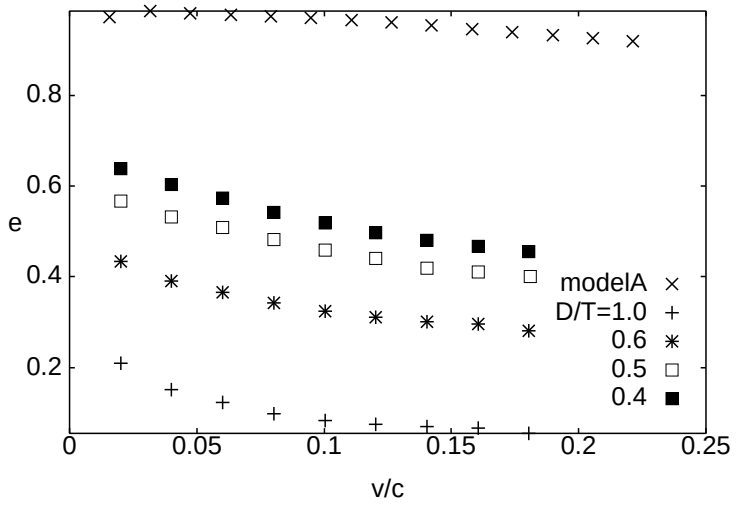

Figure 3.2: The relation between the normal impact velocity of the disk and the coefficient of restitution. Each curve has different value of D_d/T_w. The curve labeled modelA is the result in the situation when the wall has no internal degrees of freedom.

parameter made by rescaling D_d/T_w and showed that the coefficient of restitution is a function only of the impact parameter[15]. In our case, however, we could not rescale our data in order to get an universal relation between D_d/T_w and e. To clarify the reason will be one of future subject to be solved.

Chapter 4

Oblique impact of a random lattice model

In this chapter, the oblique collision between an elastic disk and an elastic wall is numerically studied. The aim of this chapter is to investigate the relation between the coefficient of tangential restitution β and the incident angle in detail from our numerical simulation using the random lattice model. Figure 4.1 is the schematic figure of an oblique impact of a disk on a wall (a) before and (b) after collision. We define γ as the incident angle in chapter 4 and 5. Here, the coefficients of normal and tangential restitution, e and β, are defined as $e = -v_n'/v_n$ and $\beta = -v_t^{(c)'}/v_t^{(c)}$, respectively. Our numerical model reproduces experimental results regarding the dependency of the coefficient of tangential restitution on the incident angle of impact and can be explained by the phenomenological theory of oblique impacts.

The organization of this chapter is as follows. In section 4.1, we introduce our numerical model and setup of the simulation. In section 4.2, we introduce Walton's simple argument of oblique collisions. Section 4.3 is the main part of this chapter where we summarize the results of our simulation and compare them with the theoretical outcome. Section 4.4 is devoted to discussion and conclusion of this chapter.

4.1 Model

Let us introduce our numerical model. Our numerical model consists of an elastic disk and an elastic wall which are based on the random lattice model in chapter 1 (Fig. 4.2). Numbers of mass particles are 1600 for both the disk and the wall. The

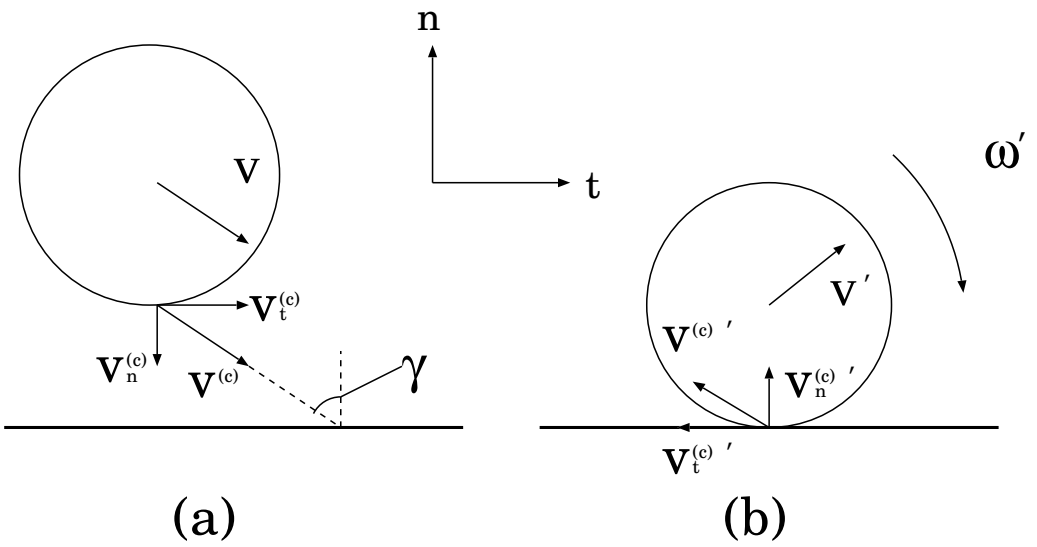

Figure 4.1: The schematic figure of a collision of a disk with a wall.

width and the height of the wall are $8R$ and $2R$, where R is the radius of the disk. We adopt the fixed boundary condition for both side ends of the wall. As for spring interactions in the model, in most of simulations, we adopt $k_a = 1.0 \times mc^2/R^2$ and $k_b = 1.0 \times 10^{-3} mc^2/R^4$ for the disk, respectively, in Eq.(1.14). For the wall, we adopt $k_a = 1.0 \times 10 mc^2/R^2$ and $k_b = 1.0 \times 10^{-3} mc^2/R^4$, respectively. As for the interaction between the disk and the wall during a collision, we adopt $a_0 = 300/R$ for the repulsive force of the disk in Eq.(1.15). All of the data presented in this chapter are obtained from the average of 100 samples in random numbers to make the roughness of the disk.

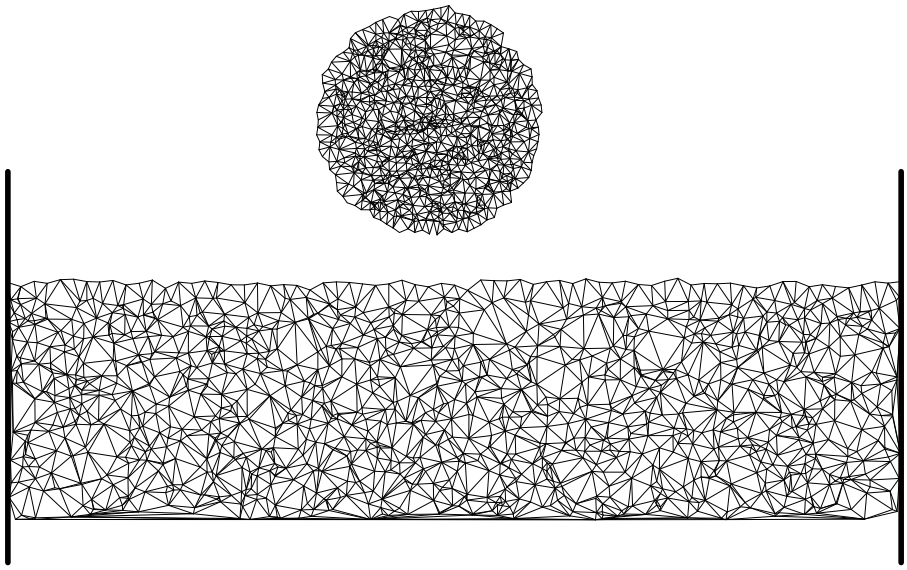

Figure 4.2: The elastic disk and wall consisted of random lattice system.

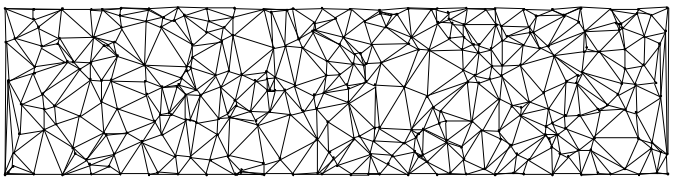

(a)

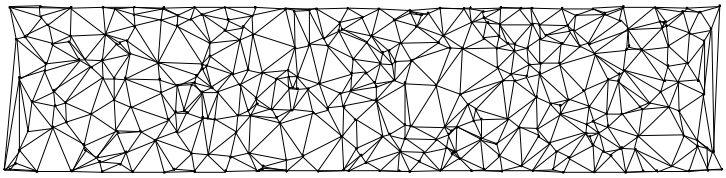

(b)

Figure 4.3: The bands of random lattice (a) before and (b) after stretch.

For the random lattice model, it is impossible to determine Poisson's ratio ν and Young's modulus E theoretically. To determine Poisson's ratio ν and Young's modulus E of this model, we add the viscous term in Eq.(1.14) which is proportional to the relative velocity of two connected mass points. By stretching the band of random lattice and calculating the ratio of the strains in vertical and horizontal directions to the force and the ratio of the vertical strain to the force when the vibration stops, we can obtain Poisson's ratio and Young's modulus. Figure 4.3(a) and 4.3(b) are snap shots of the bands of random lattice made of 348 mass points before and after adding the force $F = 3.0 \times 10^2 mc^2/R$, respectively. We change the force from $2.0 \times 10^2 mc^2/R$ to $3.0 \times 10^2 mc^2/R$ and average 10 samples of results to obtain $\nu = (7.50 \pm 0.11) \times 10^{-2}$ and $E = (9.54 \pm 0.231) \times 10^3 mc^2/R^2$, respectively.

For comparison, we introduce other two lattice models for elastic disks: triangular lattice disk and square lattice disk(Fig.4.4). To investigate the effect of the structure of the disk, the wall is same as the random lattice model. In order to remove anisotropies of the surface, we put an exterior layer of random lattice. The triangular lattice disk consists of triangular lattice in interior region and random lattice in exterior region. Total number of mass points is same as that of random disk. Poisson's ratio and Young's modulus of the triangular lattice can be calculated theoretically as $1/3$ and $2k_a/\sqrt{3}$ in the continuum limit, respectively[71].

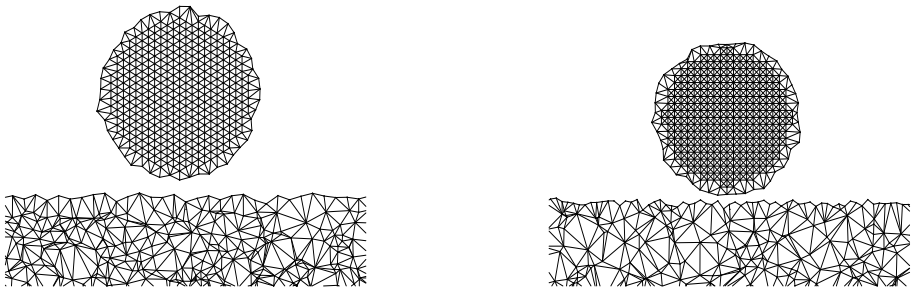

Figure 4.4: The schematic figures of (a) triangular lattice disk and (b) square lattice disk.

The square lattice disk consists of square lattice in interior region and random lattice in exterior region. We introduce two spring constants: $k_a = k_1$ for nearest neighbor interaction and $k_a = k_2$ for next-nearest neighbor interaction. In the continuum limit, Young's modulus E and Poisson's ratio ν of the square lattice are expressed as

$$\frac{1}{E} = \frac{k_1 + k_2}{k_1(k_1 + 2k_2)} + \frac{k_1 - 2k_2}{k_1 k_2} n_x^2 n_y^2, \tag{4.1}$$

$$\nu = \frac{k_2^2 + (k_1^2 - 4k_2^2) n_x^2 n_y^2}{k_2(k_1 + k_2) + (k_1^2 - 4k_2^2) n_x^2 n_y^2}, \tag{4.2}$$

where n_x and n_y are the unit normal vectors horizontal and vertical to the collisional plane.[69, 70] The derivation of Eqs.(4.1) and (4.2) is presented in appendix C. The square lattice disk is mainly used to investigate the effect of Poisson's ratio in section 4.4.

We scale the equation of motion for each particle using the radius of the disk R as the scale of length and the velocity of elastic wave $c = \sqrt{E/\rho}$ as the scale of velocity. As the numerical scheme of the integration, we use the fourth order symplectic numerical method with the time step $\Delta t \simeq 10^{-3} R/c$.

4.2 Walton's collision model

To characterize oblique collisions, Walton introduced three parameters: the coefficient of normal restitution e, the coefficient of Coulomb's friction μ_0, and the maximum value of the coefficient of tangential restitution β_0[31, 32]. Experiments have supported that his characterization adequately captures the essence of binary collision of spheres or collision of a sphere on a flat plate[4, 5, 6, 7]. Walton derives

$$\beta \simeq \begin{cases} -1 + \mu_0(1+e)\cot\gamma\left(1+\frac{mR^2}{I}\right) & (\gamma \geq \gamma_0) \\ \beta_0 & (\gamma \leq \gamma_0), \end{cases} \tag{4.3}$$

where γ_0 is the critical angle, and m, R, and I are mass, radius and moment of inertia of spheres, respectively[31, 32]. Details of the derivation are shown in appendix A. In the next section, we will compare our results with this theory and estimate the coefficient of friction of our model.

4.3 Results

In this section, we explain the results of our simulation. The angle of incidence γ is ranged from 5.7° to 80.5° while the normal component of velocity is fixed as $0.1c$. The colliding disk has no internal vibration and rotation at release time. In order to eliminate the effect of the initial configuration of mass points, we prepare 100 samples of disk as the initial condition by using 100 sets of normal random numbers and average data of all samples.

Figure 4.5 shows the relation between $\cot\gamma$ and e. Although e is expected to be a constant because the normal velocity of the disk is fixed, COR depends on γ. In particular, for small $\cot\gamma$, e decreases as $\cot\gamma$ decreases. We will discuss this behavior in the later discussion.

Figure 4.6 shows the relation between $\cot\gamma$ and the coefficient of tangential restitution β. In this figure, the cross points are the results of the impact between random lattice disk and wall, and broken lines are Eq.(4.3). In Eq.(4.3) we use the value $e = 0.8$ which is the approximate mean value of e in the range $2.5 \leq \cot\gamma \leq 6$ in Fig.4.5. The result of simulation shows that β_0 is 0.56 and μ_0 is 0.18 which are close to the values observed in experiments of three dimensional impacts[4, 5]. Thus, we reproduce experimental tendencies of the oblique collision from the simulation of the random lattice model[4, 5]. Stars are the results of random lattice disk without roughness on the surface, in which β is close to -1. From this

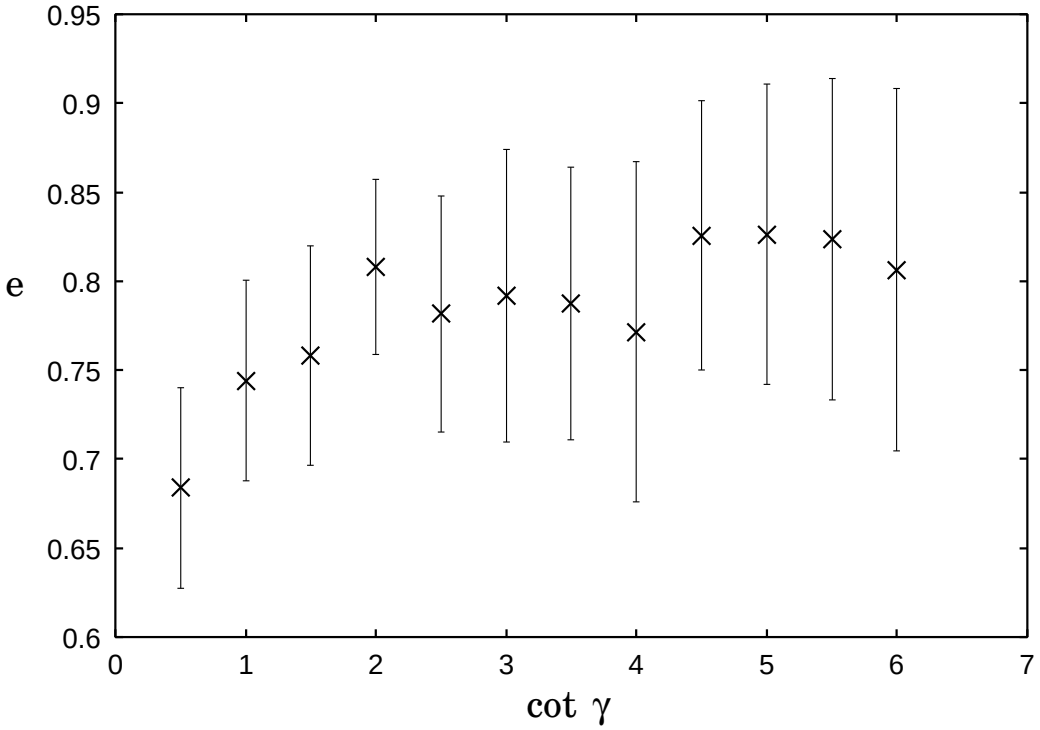

Figure 4.5: The relation between cotangent of angle of incidence γ and COR e.

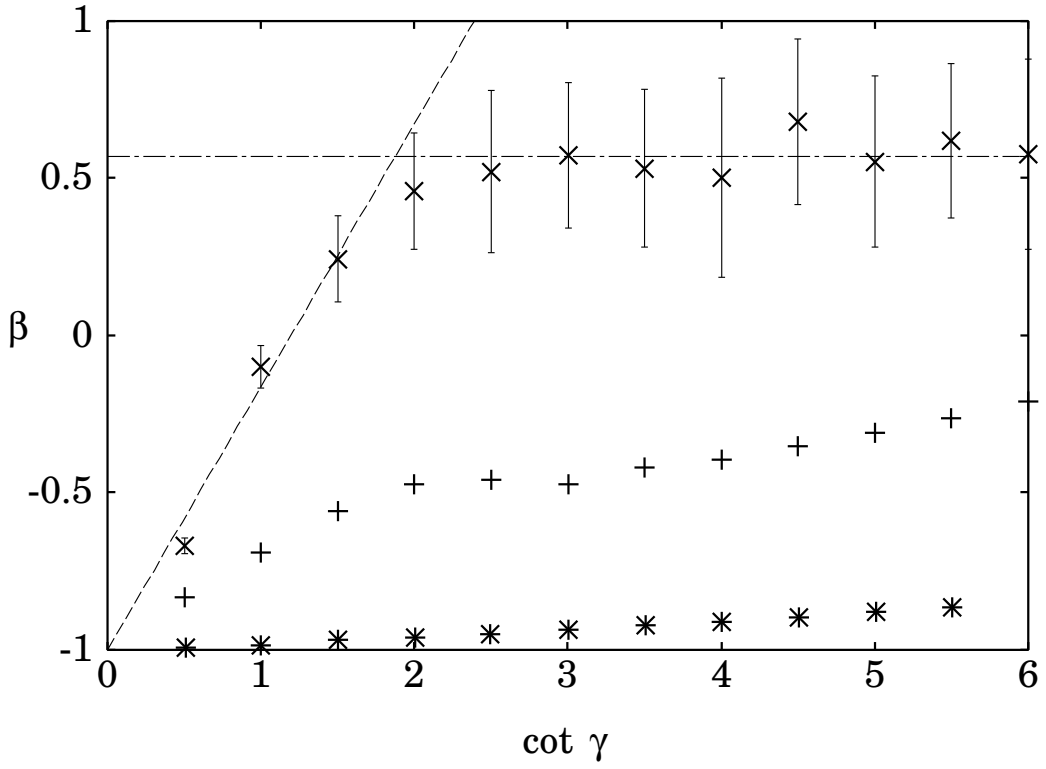

Figure 4.6: The relation between cotangent of angle of incidence γ and β. Cross points are the results of the random lattice disk. Stars are the result when the random disk has no roughness. Plus points are the results of the triangular lattice disk. Dashed and dot-dash lines are Eq.(4.3)

result, one can see that roughness on the surface is important for the rotation of the disk after collision. The plus points in Fig.4.6 are the result of the triangular lattice model where the orientation of initial disks is same as that in Fig.4.4(a). In this model, β takes negative values in all range of the angle of incidence. This means that the disk made of triangular lattice is easy to slip on the surface. In addition, the result strongly depends on the initial orientation of the disk. Thus, the model of triangular lattice is inadequate to reproduce the tendency of experimental data.

Here, we compare our result with the theory of Maw *et al.*[27, 28, 29] which can reproduce experimental data[5, 6, 7, 27, 28]. Details of the derivation of the theory are shown in appendix B. According to their theory, all the region of the angle of incidence can be divided into three regimes. For each regime, β can be expressed as

(i) $1/\mu\eta^2 < \cot\gamma$:

$$\beta = -\cos\omega t_1 - \mu\frac{\beta_x}{\beta_z}e\left[1+\cos\left(\frac{\Omega t_1}{e}+\frac{\pi}{2}(1-e^{-1})\right)\right]\cot\gamma, \tag{4.4}$$

(ii) $\beta_x/\beta_z\mu(1+e) < \cot\gamma < 1/\mu\eta^2$:

$$\begin{aligned}\beta = &-\cos\omega(t_3-t_2) - \mu\frac{\beta_x}{\beta_z}[\cos\omega(t_3-t_2) - \cos\Omega t_2\cos\omega(t_3-t_2)\\ &+\frac{\Omega}{\omega}\sin\Omega t_2\sin\omega(t_3-t_2)+e+\cos\Omega t_3]\cot\gamma,\end{aligned} \tag{4.5}$$

(iii) $\cot\gamma < \beta_x/\beta_z\mu(1+e)$:

$$\beta = -1+\mu\frac{\beta_x}{\beta_z}(1+e)\cot\gamma, \tag{4.6}$$

where μ is the coefficient of friction, η is the constant dependent on Poisson's ratio defined in Eq.(B.5), β_x and β_z are constants calculated from mass, radius, and radii of gyration of material as $\beta_x = 3.02$ and $\beta_z = 1$. Ω and ω are respectively $\pi/2t_c$ and $(\pi/2\eta t_c)\sqrt{\beta_x/\beta_z}$, where t_c is the time when compression terminates. In the regime (i), the disk initially sticks and starts to slip at $t = t_1$ which is determined by Eq.(B.10). In the regime (ii), the initial sliding motion of the disk continues until $t = t_2$ which is determined by Eq. (B.20). After the sticking period, the disk starts to slide again at $t = t_3$ which is determined by Eqs.(B.21). By calculating β at each value of $\cot\gamma$ and interpolating them with cubic spline interpolation method, we can draw the theoretical curve.

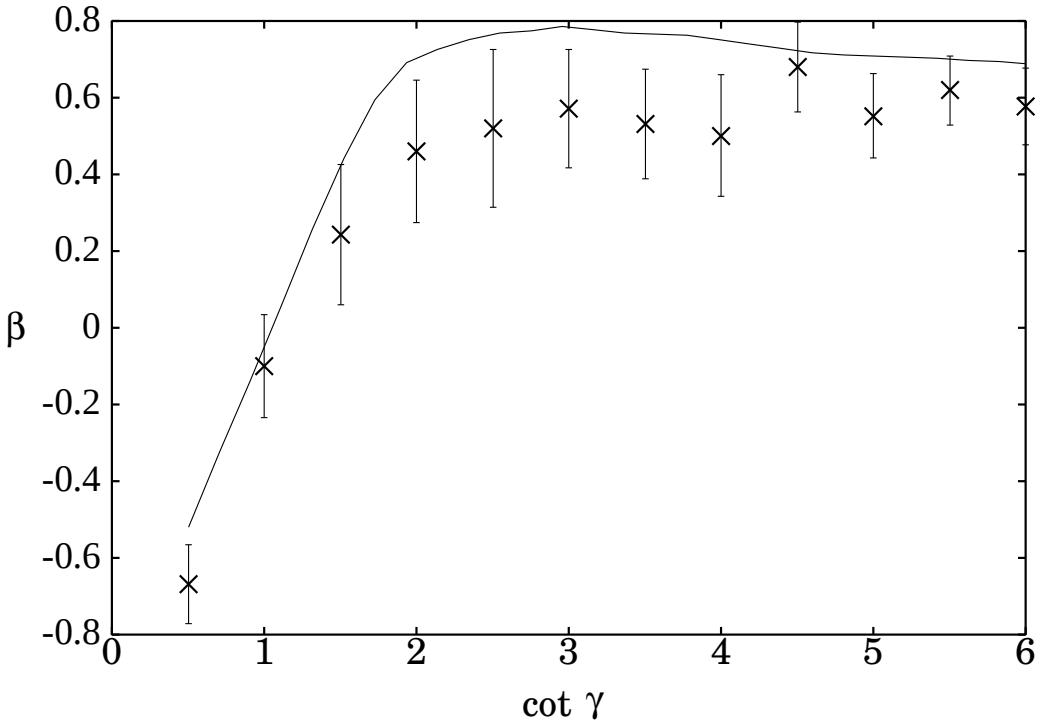

Figure 4.7: The relation between $\cot\gamma$ and β. Cross points are the numerical results of the random lattice model. Solid line is the theoretical curve.

We compare the result of simulation of the oblique impact using the random lattice model with the theoretical curve(Fig.4.7). Here we used $\eta = 1.015$, $e = 0.8$ which is an average value of COR in Fig.4.5, and $\mu = 0.18$ which is decided by comparing the slope in the small $\cot\gamma$ region with Eq.(4.3). It is found that the result of random lattice model is consistent with the theory especially in small $\cot\gamma$ region. In the intermediate region, the agreement of the data with the theory is worse than that of other regions. This tendency can be seen in some experimental results [5, 7, 28].

Theoretical result by Maw *et al.* suggests that Poisson's ratio is not a crucial parameter to determine β_0, while Poisson's ratio of the triangular lattice is much larger than that of the random lattice. To confirm that anomalous behavior of the triangular lattice comes from the specific lattice structure, we simulate the collision by using the square lattice model. By changing the value of spring constants of square lattice disk and controlling Poisson's ratio, we investigate the depen-

dency of β_0 on Poisson's ratio. β_0 are 0.49 and 0.51 when $\nu = 0.1$ and $\nu = 0.3$, respectively. From these results, we confirm that Poisson's ratio is not a crucial parameter for β_0.

4.4 Discussion and conclusion

Here, we discuss the results of our simulation. We change the number of mass points of random lattice model and investigate the dependency on the system size. As the number of mass points becomes larger, there is a tendency for a graph to be flattened in the region of large $\cot\gamma$. It can be seen as follows. When the model is composed of many mass points, irregularity of the surface of the random lattice diminishes as the size of the disk increases. As a result, β_0 can take a stable value in the large $\cot\gamma$. When the number of mass points is larger than 1600, all the mass points in the rectangle cannot be connected by the Delaunay triangulation algorithm[75]. Hence, our results are restricted to the case with the 1600 mass points as the maximum value.

We also investigate the influence of roughness of the surface. When the standard deviation δ takes $2.15 \times 10^{-2}R$, β shows monotonic increase with increasing $\cot\gamma$. When δ takes $3.0 \times 10^{-3}R$, β approaches the stable maximum value $\beta_0 = 0.56$. For larger δ, the surface of the rectangle is easy to collapse when the collision occurs. As for the coefficient of friction μ_0, μ_0 takes 0.14 when δ is $2.15 \times 10^{-2}R$ while μ_0 takes 0.18 when δ is $3.0 \times 10^{-2}R$. It can be seen that roughness of the surface make the value of μ_0 increase.

The random lattice model can reproduce experimental tendency in β_0 and μ_0 with roughness on the surface. However, the random lattice model cannot reproduce the tendency that β decreases from the maximum value β_0 in the large $\cot\gamma$[4]. Other mechanisms like sticking or plastic deformation on the surface may be important in the large γ region.

From Fig.4.6, the triangular lattice disk seems to be inadequate to reproduce experimental tendency. The polygonal property of the structure in the triangular lattice disk may cause the slip motion of the disk.

The decrease of e in the small $\cot\gamma$ in Fig.4.5 can be understood as follows. In our situation, normal component of initial velocity is fixed to $0.1c$. Thus, the initial kinetic energy of the disk becomes larger in the small $\cot\gamma$. As a result, the surface of the wall cannot seize the disk so that the initial kinetic energy is easy to propagate in the horizontal direction to the surface of the wall.

In the last section we investigated the dependency on Poisson's ratio with the

aid of the square lattice model. In contrast, we change the value of k_a of the triangular lattice disk from $1.0 \times mc^2/R^2$ to $1.0 \times 10^2 mc^2/R^2$ to investigate the dependency on Young's modulus. Although Young's modulus increases by 100-fold, the triangular lattice disk remains slippery on the surface. From this fact, it can be seen that Young's modulus as well as Poisson's ratio are not crucial. In addition, we change the value of k_b of triangular lattice disk from $1.0 \times 10^{-3} mc^2/R^4$ to $1.0 \times 10^{-1} mc^2/R^4$ and investigate the effect of the nonlinear term of Eq.(1.14). The change of k_b also does not affect the results of triangular lattice disk. It can be seen that the nonlinear term of Eq.(1.14) only strengthen the surface of the model and does not make the triangular lattice disk rotate after collision. In the triangular lattice disk, the polygonal property of the surface of triangular lattice may affect the results.

Finally, we refer to the connection between μ_0 in Eq.(4.3) and μ in Eq.(4.6). In Fig.4.7, the value of μ is same as μ_0 estimated from the slope in the range $0 \leq \cot\gamma \leq 2$ in Fig.4.6. Comparing Eq.(4.3) with Eq.(4.6), we can derive the relation between μ_0 and μ as

$$\mu \frac{\beta_x}{\beta_z} = \mu_0 \left(1 + \frac{mR^2}{I} \right). \tag{4.7}$$

In the two dimensional binary collision of disks, $1 + mR^2/I$ can be calculated as 3 explicitly. Meanwhile, β_x/β_z in our system can be calculated as 3.02. Thus, μ and μ_0 are in our case almost identical.

In this chapter, we have demonstrated the two-dimensional simulation of the oblique impact. Our random lattice model produces the same tendency as experimental data qualitatively while triangular lattice model can not produce the positive value of β_0. For normal COR, e depends on the initial angle of incidence and decreases in the large γ when the normal component of initial velocity is fixed. For β, we compare our results with Maw's theory of the oblique impact. Our result is consistent with their theory especially in the large and small region of $\cot\gamma$.

Chapter 5

Oblique impact of an elastic disk on a soft wall

In this chapter, we demonstrate that COR increases with $\tan\gamma$ to exceed 1 at the critical incident angle through in our two-dimensional simulation of the oblique impact between an elastic disk and an elastic wall[74]. As related in chapter 1, it is recently reported that COR can exceed unity in oblique impacts[42, 43, 30] while COR has been believed to be less than 1 in most situations. In the next section, we construct an impact model by extending the model in the previous chapter. In section 5.2 and 5.3, we will show the relation between e and the tangent of incident angle and the relation between μ and the tangent of incident angle and explain our results with the aid of the theory of elasticity[51, 78]. The final section is devoted to the discussion and conclusion of this chapter.

5.1 Model

Let us introduce our numerical model[79]. Our numerical model consists of an elastic disk and an elastic wall (Fig. 5.1). The width and the height of the wall are $8R$ and $2R$, respectively, where R is the radius of the disk. We adopt the fixed boundary condition for the both side ends and the bottom of the wall. To make each of them, at first, we place mass points at random in a circle and a rectangle with the same density, respectively. We place 800 mass points at random in a circle with the radius R for the disk while we place 4000 mass points at random in a rectangle for the wall.

We connect all the mass points with nonlinear springs for each of them using

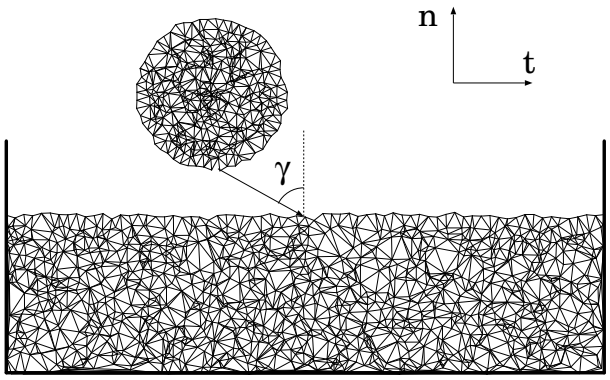

Figure 5.1: The elastic disk and the elastic wall consisted of random lattice.

the Delaunay triangulation algorithm[75]. The spring interaction between connected mass points is given by

$$V^{(i)}(x) = \frac{1}{2}k_a^{(i)}x^2 + \frac{1}{4}k_b^{(i)}x^4, \quad i = d(\text{disk}), w(\text{wall}), \tag{5.1}$$

where x is a stretch from the natural length of the spring, and $k_a^{(i)}$ and $k_b^{(i)}$ are the spring constants for the disk(i=d) and the wall(i=w). In most of our simulations, we adopt $k_a^{(d)} = 1.0 \times mc^2/R^2$, $k_a^{(w)} = k_a^{(d)}/100$, and $k_b^{(i)} = k_a^{(i)} \times 10^{-3}/R^2$, where m and c are the mass of each mass point and the one-dimensional velocity of sound, respectively. We do not introduce any dissipation mechanism in this model. The interaction between the disk and the wall during a collision is introduced as follows. The lower surface mass points of the disk are reflected by the force, $\mathbf{F}(l_s) = aV_0 \exp(-al_s)\mathbf{n}^s$, where a is $300/R$, V_0 is $amc^2R/2$, l_s is the distance between each surface mass point of the disk and the nearest surface spring of the wall, and $\mathbf{n}^s$ is the normal unit vector to the spring [79]. We should note that the strong repulsion force $\mathbf{F}(l_s)$ is introduced to inhibit the penetration of mass points of the disk to the surface springs of the wall[37]. We have confirmed that the model reproduces two-dimensional Hertzian contact theory by adding gravity and dissipation.

In this model, the roughness of surfaces is important to make the disk rotate after a collision[79]. To make roughness, we displace the surface mass points of both the disk and the wall by generating normal random numbers with its average and standard deviation, 0 and $3 \times 10^{-2}R$, respectively. All the data in this letter are obtained from the average of 100 samples in random numbers.

Poisson's ratio ν and Young's modulus E of this model can be evaluated from the strains of the band of random lattice in vertical and horizontal directions to the applied force. We obtain Poisson's ratio ν and Young's modulus E as $\nu = (7.50 \pm 0.11) \times 10^{-2}$ and $E = (9.54 \pm 0.231) \times 10^{3} mc^2/R^2$, respectively.

We fix the initial colliding speed of the disk $|\mathbf{v}(0)|$ as $0.1c$ and set the tangential and the normal components as $v_t(0) = |\mathbf{v}(0)| \sin\gamma$ and $v_n(0) = |\mathbf{v}(0)| \cos\gamma$, respectively. After a collision, we calculate COR for each γ. We use the fourth order symplectic numerical method for the numerical scheme of integration with the time step $\Delta t = 10^{-3}R/c$.

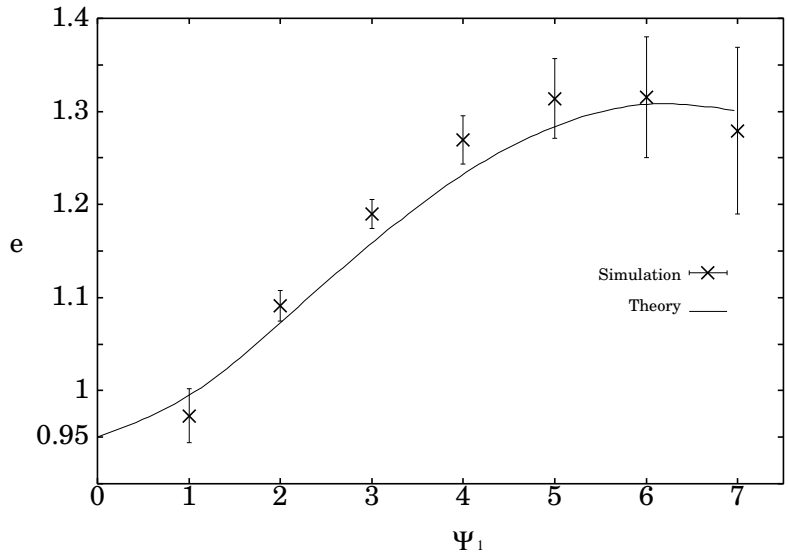

Figure 5.2: Numerical and theoretical results of the relation between Ψ_1 and COR.

5.2 e vs. Ψ_1

Figure 5.2 is the relation between COR and $\Psi_1 = -(\mathbf{v}(0) \cdot \mathbf{t})/(\mathbf{v}(0) \cdot \mathbf{n}) = \tan\gamma$ obtained from our simulation. The cross point is the mean value and the error bar is the standard deviation of 100 samples for each γ. This result shows that COR increases with increasing Ψ_1 to exceed unity, and has a peak around $\Psi_1 = 6.0$. The behavior of e having the peak is contrast to that in the experiment by Louge and Adams[30].

Here, let us clarify the mechanism of our results. Louge and Adams[30] interpret that e exceeds 1 in terms of the local deformation of the wall surface during an impact. They suggest that their results can be explained by the rotation of normal unit vector of the wall surface by an angle α. Thus, we determine α at each γ from the theory of elasticity.

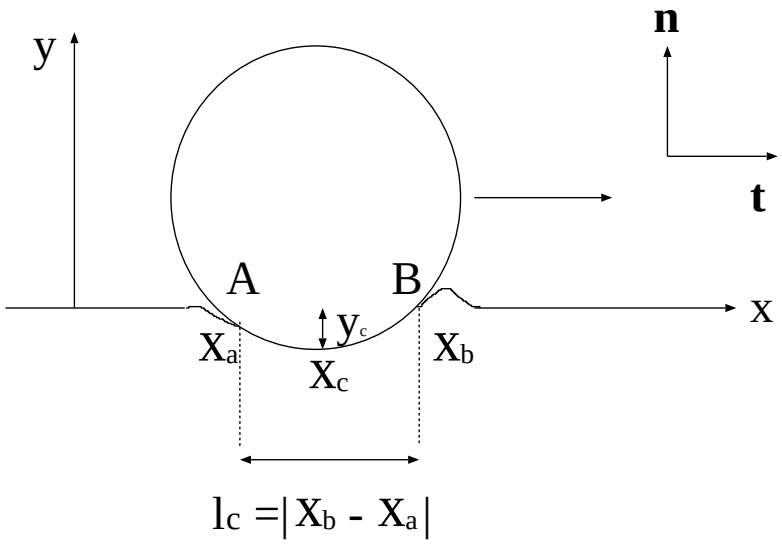

Figure 5.3: The schematic figure of a hard disk sliding on a soft wall. x coordinates of both ends of the contact area AB are $x = x_a$ and $x = x_b$.

Figure 5.3 is the schematic figure of a hard disk moving from left to right on a wall, where the length of the contact area is $l_c = |x_b - x_a|$. We introduce the horizontal unit vector of the wall surface as $\mathbf{t}$. Assuming that the contact area is small in comparison with the radius of the disk R, we approximate the contact

area by the parabola

$$f(x) = (x - x_c)^2/2R - y_c, \tag{5.2}$$

where (x_c, y_c) corresponds to the contact point of the disk. In this situation, $\tan\alpha$ is defined by $\tan\alpha = (f(x_b) - f(x_a))/l_c$. To calculate $\tan\alpha$, we need to know the ratio of $|x_c - x_a|$ to l_c. From the theory of elasticity[51, 78], this ratio can be estimated as

$$\frac{x_c - x_a}{l_c} = 1 - \theta \quad \text{with} \quad \theta = \frac{1}{\pi}\arctan\frac{1-2\nu}{\mu(2-2\nu)}, \tag{5.3}$$

where ν is Poisson's ratio of the wall and μ is the coefficient of friction. Note that Eq.(5.3) equals to $1/2$ when $\mu = 0$. From Eqs.(5.2) and (5.3), $\tan\alpha$ is given by

$$\tan\alpha = \frac{2\theta - 1}{2 - 2\theta}\frac{|x_c - x_a|}{R}. \tag{5.4}$$

In Eq.(5.4), $|x_c - x_a|$ can be evaluated by the simulation data. We adopt $|x_c - x_a| = 0.55R$ from the maximum value of the compression of the disk.

To evaluate α, we need to evaluate the coefficient of friction μ through the definition $\mu = |\mathbf{J}\cdot\mathbf{t}|/|\mathbf{J}\cdot\mathbf{n}|$, where $\mathbf{J} = m(\mathbf{v}(t_f) - \mathbf{v}(0))$ and t_f is the duration. The cross points in Fig.5.4 represent μ calculated from our simulation data. Figure 5.4 shows μ has a peak around $\Psi_1 = 3.0$. Substituting this result to Eq.(5.4), we obtain the relation between Ψ_1 and $\tan\alpha$.

Next, let us calculate COR on a tilted surface. We introduce the normal and tangential unit vectors on the contact area, $\mathbf{n}_\alpha$ and $\mathbf{t}_\alpha$, as $\mathbf{n}_\alpha = \cos\alpha\mathbf{n} - \sin\alpha\mathbf{t}$ and $\mathbf{t}_\alpha = \sin\alpha\mathbf{n} + \cos\alpha\mathbf{t}$, respectively. By introducing $e_\alpha \equiv -(\mathbf{v}(t_f)\cdot\mathbf{n}_\alpha)/(\mathbf{v}(0)\cdot\mathbf{n}_\alpha)$, we can express e in terms of e_α as

$$e = \frac{e_\alpha + \Psi_2^\alpha\tan\alpha}{1 - \Psi_1^\alpha\tan\alpha}, \tag{5.5}$$

where $\Psi_1^\alpha = -(\mathbf{v}(0)\cdot\mathbf{t}_\alpha)/(\mathbf{v}(0)\cdot\mathbf{n}_\alpha)$ and $\Psi_2^\alpha = -(\mathbf{v}(t_f)\cdot\mathbf{t}_\alpha)/(\mathbf{v}(0)\cdot\mathbf{n}_\alpha)$. Ψ_1^α can be rewritten as

$$\Psi_1^\alpha = (\Psi_1 - \tan\alpha)/(1 + \Psi_1\tan\alpha). \tag{5.6}$$

On the other hand, in the oblique impact of hard disks accompanied by gross slip on the surface, Ψ_2^α is represented by

$$\Psi_2^\alpha = \Psi_1^\alpha - 3(1 + e_\alpha)\mu_\alpha \tag{5.7}$$

in the two-dimensional situation[31]. In Eq.(5.7), μ_α is defined by $\mu_\alpha = |\mathbf{J} \cdot \mathbf{t}_\alpha|/|\mathbf{J} \cdot \mathbf{n}_\alpha|$ and expressed as

$$\mu_\alpha = \frac{\mu + \tan\alpha}{1 - \mu\tan\alpha}. \tag{5.8}$$

Here, μ_α is the coefficient of sliding friction without deformation of the wall. To draw the solid line in Fig.5.2, at first, we calculate μ and $\tan\alpha$ respectively for each Ψ_1. Then, we calculate Ψ_1^α and Ψ_2^α by Eqs.(5.6) and (5.7), and obtain e by substituting them into Eq.(5.5) for each Ψ_1. We assume e_α is a constant less than 1. The solid line of Fig.5.2 is Eq.(5.5) with $e_\alpha = 0.95$ which is the value in the normal impact. All points are interpolated with cubic spline interpolation method to draw the theoretical curve. Such the theoretical description of e is qualitatively consistent with our numerical result, though the theoretical value is smaller than the observed value.

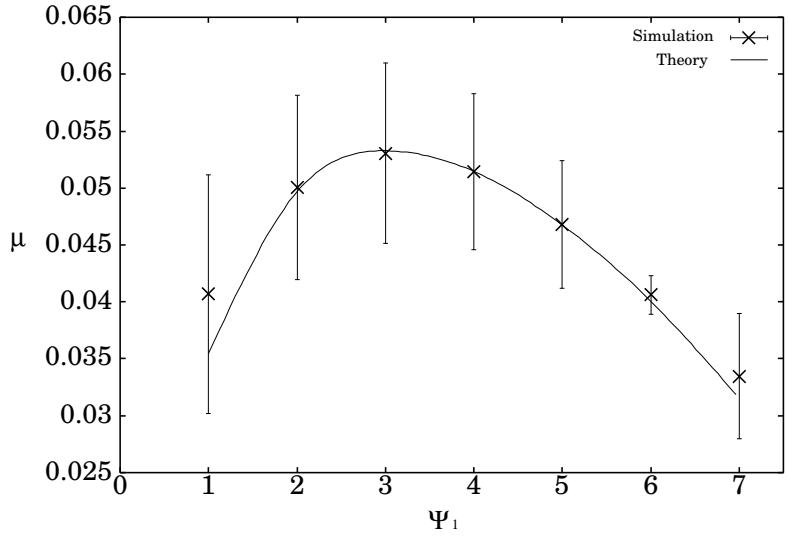

Figure 5.4: Numerical and theoretical results of the relation between Ψ_1 and μ.

5.3 μ vs. Ψ_1

Finally, we explain the dependence of μ upon Ψ_1 by a phenomenological theory. In our model, the roughness at the surfaces of the wall and the disk is

important[79]. We assume that the tangential velocity of the disk is decreased by η_t when the disk interacts with one jag on the surface of the wall. The length that the disk slides within a duration is estimated as $v_t(0)t_f \simeq v_t(0)\pi(R/c)\sqrt{\ln(4c/v_n(0))}$, where we use the expression of t_f in Ref.[39]. Assuming that jags are placed on the surface of the wall uniformly and have same size, the tangential velocity after collision is calculated as $v_t(t_f) = v_t(0) - \eta\rho v_t(0)\pi(R/c)\sqrt{\ln(4c/v_n(0))}$, where ρ is the number of jags on the unit length. The tangential impulse J_t is given by

$$J_t = -m\eta\rho|\mathbf{v}(0)|\sin\gamma\pi\frac{R}{c}\sqrt{\ln\left(\frac{4c}{|\mathbf{v}(0)|\cos\gamma}\right)} \tag{5.9}$$

while the normal impulse is given by $J_n = -m(e+1)|\mathbf{v}(0)|\cos\gamma$, where we use $v_n(t_f) = -ev_n(0)$. We assume that the tangential impulse decreases by $J_t^{'} = -m\zeta|\mathbf{v}(0)|\sin\gamma$, where ζ is a proportionality constant, from the effect of the local deformation of the wall. Thus, μ can be represented by the ratio of $|J_t - J_t^{'}|$ to $|J_n|$ as

$$\mu = \left|\zeta\tan\gamma - \eta_t\rho\tan\gamma\pi\frac{R}{c}\sqrt{\ln\left(\frac{4c}{|\mathbf{v}(0)|\cos\gamma}\right)}\right|/(e+1). \tag{5.10}$$

In this expression, e is the cross point in Fig.5.2 for each Ψ_1. ζ and $\eta_t\rho$ are fitting parameters. The solid curve in Fig.5.4 is Eq.(5.10) with fitting parameters, $\zeta = 0.397$ and $\eta_t\rho = 0.163c/R$, which reproduces our numerical result. We do not claim that our simple argument explains the experimental result because of some fitting parameters. However, we would like to emphasize that our picture captures the essence of the physics of impact.

5.4 Discussion and conclusion

Let us discuss our result. First, we emphasize that the novel phenomena of e exceeding unity are obtained from the local deformation of wall for the oblique impacts of a hard disk on a soft wall. When we simulate the impact between a disk and a hard wall, when $k_a^{(w)} = 10 \times k_a^{(d)}$, e takes almost constant value to exceed unity abruptly around $\Psi_1 = 4.5$(Fig. 5.5). This tendency resembles the experimental results by Calsamiglia *et al.*[43]. Thus, for smooth increase of e to exceed unity, the wall should be softer than the disk. In addition, it is important to fix the initial kinetic energy of the disk. So far, we have confirmed that e does

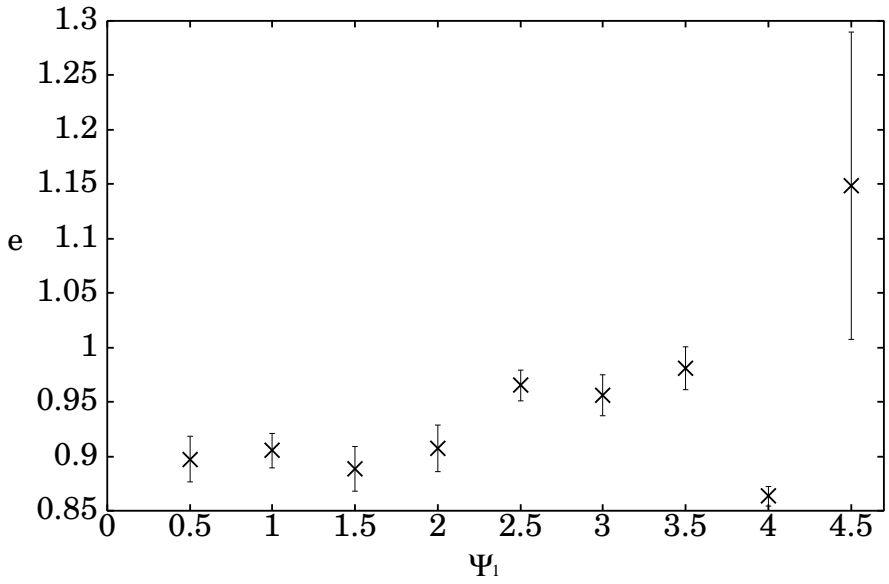

Figure 5.5: The relation between Ψ_1 and μ in the case of hard wall.

not exceed unity when Ψ_1 is controlled by changing v_t with fixed v_n[79]. In that case, the initial kinetic energy of the disk becomes large for the large Ψ_1 so that the local deformation of the wall is easy to collapse in the grazing collision.

The second, the initial velocity of the disk and the local deformation of the wall are much larger than those in the experimental setup in Ref.[30]. This is the most significant difference between our result and that by Louge and Adams. Because of the high speed impact, there is a peak of e for small γ. In fact, out simulation with $v = 0.01c$ shows the shift of the peak for larger γ. Therefore, we expect that our model reproduces the result of Ref.[30] for low impact speed. In addition, we have carried out other simulation with a disk of 400 mass points and a wall of 2000 mass points to investigate the effect of the system size. Although there is a slight difference between the results, the data can be also reproduced quite well by our phenomenological theory.

The third, the local deformation of the wall also affects the relation between μ and Ψ_1. In early studies, it has been shown that μ depends on the impact velocity [7, 30]. In our simulation, the magnitude of α has a peak around $\Psi_1 = 3.0$. This behavior is interpreted as that the local deformation collapses with large v_t. We derived in this letter the relation between μ and Ψ_1 by Eq.(5.10). By control-

ling ζ and $\eta_t\rho$, Eq.(5.10) shows monotonic increase like the result of Louge and Adams[30](see Fig.5.10). The difference between the results of their experiment

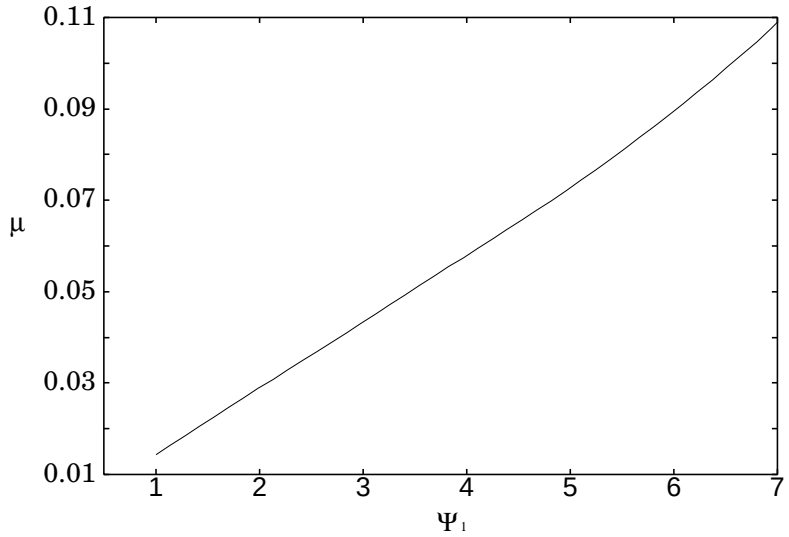

Figure 5.6: The relation between Ψ_1 and μ in the case of $\zeta = 0$ and $\eta\rho = 0.014c/R$ in Eq.(5.10).

and our simulation may be explained by the choice of these parameters.

Fourthly, we draw the solid line in Fig. 5.2 on the assumption that $e^\alpha = 0.95$. When we calculate e^α in Eq. (5.5) from the definition $e^\alpha = -(\mathbf{v}(t_f)\cdot\mathbf{n}_\alpha)/(\mathbf{v}(0)\cdot\mathbf{n}_\alpha)$, the comparison between our numerical results and Eq. (5.5) becomes as Fig. (5.7). Also in this case, the agreement seems to be fair.

In final, we adopt the static theory of elasticity to explain our numerical results in this chapter. However, it is important to solve the time-dependent equation of the deformation of the wall surface to analyze the dynamics of impact phenomena. The dynamical analysis is our future task.

In summary, we have carried out the two-dimensional simulation of the oblique impact of an elastic disk on an elastic wall. We have found that COR can exceed unity in the oblique impact, which is attributed to the local deformation of the wall. We have estimated the magnitude of the local defomation α based upon the static theory of elasticity and derived the relation between e and Ψ_1 by taking into account the rotation of the normal unit vector of the wall surface. The relation between μ and Ψ_1 is also related to the local deformation and explained by the

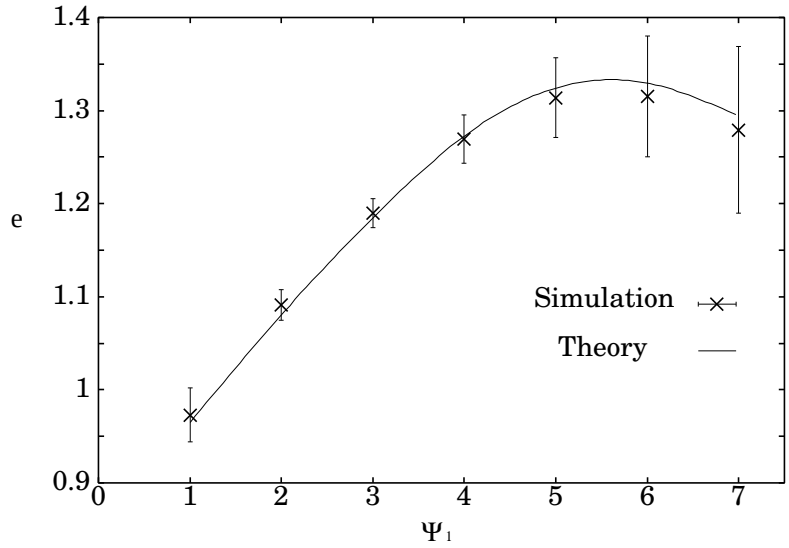

Figure 5.7: Numerical and theoretical results of the relation between Ψ_1 and e when e^α is not a constant.

simple analysis assuming the decrease of the tangential impulse proportional to the initial tangential velocity of the disk.

Chapter 6

General discussion

In the dissertation, we carried out two-dimensional simulation for both normal and oblique collisions of elastic disks on elastic walls. We confirmed that our numerical model can reproduce some experimental results and phenomenological theory. Here, we give a general discussion of our analysis.

Through the dissertation, we used the numerical model based on mass-spring model[68], although there exist some numerical models like FEM. Our model is intuitive and easy to modify the initial condition. However, the model has disadvantages that calculation takes long times as the number of mass points increases, and the numerical result strongly depends on lattice structures. The number of mass points is in the range between 1000 and 5000. As shown in chapter 4 and 5, the number of mass points in the random lattice model is adequate to reproduce the experimental results. The triangular lattice model and square lattice model cannot reproduce the experimental results although they have same number of mass points. This difference may be attributed to the polygonal shape of the surface due to poor number of mass points. The regular lattice model with adequate number of mass points may reproduce experimental results as in the case of the random lattice model.

In addition, we performed two-dimensional simulation in this dissertation. We also need to perform three-dimensional simulation to compare the numerical results with experimental results. When we extend our model to three-dimensional model, the results may completely differ because elastic wave after collision will propagate in three-dimensional directions. To construct three-dimensional numerical model is our future task.

We started this work to investigate the dominant mechanism of energy dissipation in inelastic impacts originally. The present model can reproduce some

experimental results although it does not contain energy dissipation mechanism such as viscosity. In chapter 5, we have attempted to introduce dashpots in the spring interaction as the maxwell model of viscoelasticity. However, there is little difference between results in both cases. This may be attributed to the large impact velocity such as $v = 0.1c$. Similarly, it has become clear that the existence of gravitational field does not affect our numerical results. In the range of small impact speed, the effect of such mechanisms may become prominent.

In the dissertation, we did not discuss thermal conduction arisen from inelastic impact while we discussed the effect of initial temperature of colliding material. In the analysis of Gerl *et al.*[37] and Morgado *et al.*[34], they carried out the analysis based on the assumption that the colliding disk is uniformly thermalized in the duration. However, it is clear that there exists thermal conduction during impact. For example, in Ref. [16], it is shown that an increase in temperature is produced at contact point in the experiment of binary collision of metal. It is also shown that temperature rise is higher when curvature radius of colliding material is small. It seems to be interesting to investigate numerically and theoretically the amount of energy transformed into heat during collision.

In chapter 2, we compared our numerical results with the analysis based on plastic deformation [24, 25] although our model does not include the mechanism of plastic deformation. We regarded the irreversible deformed state after collision (see Fig. 2.10(a)) as plastic deformation. It may be needed that we include the mechanism of plastic deformation, such as breaking rule for springs, in our model and compare numerical results with the theory.

In chapter 5, we explained the relation between the incident angle and the coefficient of friction based on the static theory of elasticity. Our analysis is based on the assumption that static theory is valid at any instance in the dynamic impact process. We need to represent the dynamics of the wall under impact and compare the result with numerical results.

In chapter 4 and chapter 5 we have carried out impact simulation using the random lattice model. However, we have not shown the reliability of the model although we have shown its consistency with early experimental results and phenomenological theories. In the next sections, we will discuss the reliability of the model by comparing with the existing theory introduced in this dissertation.

6.1 Comparison with the Hertzian contact theory

Here we introduce dissipation in the model and let the disk be in contact with the wall. We measure the relation between the compressive force $\mathbf{P}$ and the macroscopic deformation ξ to compare the results with the two-dimensional contact theory of Hertz.

As shown in chapter 1, the relation between the compressive force $\mathbf{P}$ and the macroscopic deformation ξ of spherical bodies in contact is represented by $\xi \propto \mathbf{P}^{2/3}$ in three-dimensional situation[49]. In contrast, in two-dimensional situation, the relation between the compressive force $\mathbf{P}$ and the macroscopic deformation ξ is represented by

$$\xi \simeq b\frac{P}{\pi E}\left(ln\left(\frac{4\pi ER}{bP}-1\right)\right), \quad b = 1-\nu^2 \tag{6.1}$$

where E is Young's modulus, ν is Poisson's ratio, and R is radius of a disk[37]. In our model, b is nearly equal to 1 because of $\nu = 0.075$ in our case.

At first, we put the disk in a gravitational field. The wall is expressed by an exponential function. In this situation, equation of motion for i-th mass point is described as

$$m\frac{d^2\mathbf{r}_i}{dt^2} = \sum_{j=1}^{N_i}\left\{-k_a\mathbf{x}_{ij} - k_b\mathbf{x}_{ij}^3 - \eta_{dis}(\mathbf{v}_i-\mathbf{v}_j)\right\} + aV_0\exp(-ay_i)\hat{\mathbf{y}} - \frac{\mathbf{P}}{N}\hat{\mathbf{y}}, \tag{6.2}$$

where $\mathbf{v}_i$ is the velocity of i-th mass point and N is a total number of mass points. Here we used $\eta_{dis} = 1.0\times 10^2 M/(R/c)$ which is introduced to relax vibrational motion of the disk, and $N = 1099$. After a period of initial oscillation the disk reaches a static state (see Fig.6.1). We changed the value of $\mathbf{P}$ from $4.0\times 10^{-3}mc^2/R$ to $1.0\times 10^{-2}mc^2/R$ and measured macroscopic deformations ξ which is defined by $|R-R^{'}|$, where $R^{'}$ is the distance from the center of the disk to the contact patch.

Figure 6.2 is the relation between $\mathbf{P}$ and ξ in which the cross points are our numerical results and the solid line is Eq.(6.1) with $b = 1.55$. If we take more sample by changing configuration of mass points in the disk and average the data, data may be fitted precisely with more adequate fitting parameters. However, we would like to emphasize that our results can be fitted by the two-dimensional Hertzian theory.

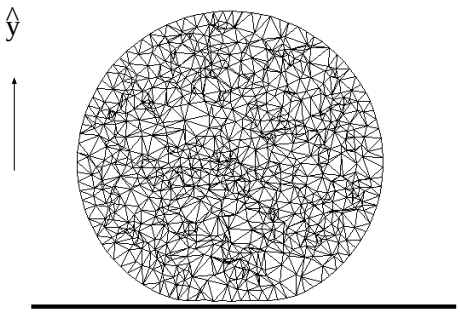

Figure 6.1: The disk is in contact with a potential wall

6.2 Comparison with quasi-static theory

Here we demonstrate the normal impact of the disk on the potential wall with low impact speed and compare the results with quasi-static theory[26]. In the two-dimensional case, as is shown in Eq.(1.12), COR may be expressed by

$$e \simeq d_1 \sqrt{1 - \frac{d_2}{\sqrt{\ln(4c/v)}}}, \tag{6.3}$$

where $d_1 = 1$ and $d_2 = 2\pi\tau_0 E_*/(\rho R c)$.

We solve equation of motion for each mass point of the disk,

$$m\frac{d^2\mathbf{r}_i}{dt^2} = \sum_{j=1}^{N_i} \left\{ -k_a \mathbf{x}_{ij} - k_b \mathbf{x}_{ij}^3 - \eta_{dis}(\mathbf{v}_i - \mathbf{v}_j) \right\} + aV_0 \exp(-ay_i)\hat{\mathbf{y}} \tag{6.4}$$

with initial velocity from $3.0\times10^{-3}R/c$ to $5.0\times10^{-2}R/c$ and calculate coefficient of restitution for each initial velocity. We adopted $\eta_{dis} = 100m/(R/c)$.

Figure 6.3 is the relation between initial velocity and coefficient of restitution. The data are fitted by Eq.(6.3) with $d_1 = 1.24$ and $d_2 = 1.08$. If we take more

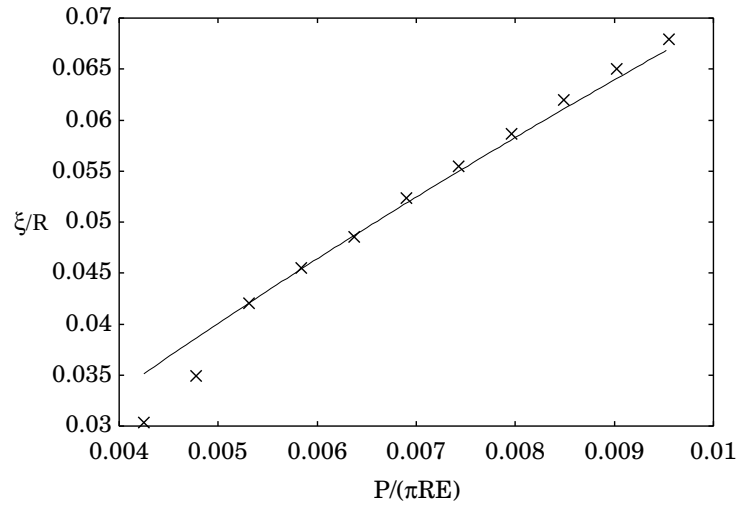

Figure 6.2: The relation between the compressive force and the macroscopic deformation

sample by changing configuration of mass points in the disk, data may be fitted precisely with more adequate fitting parameters. Here, we would like to claim that our data can be fitted by the quasi-static theory. This is also indirect support of our model which is consistent with the Hertzian contact theory.

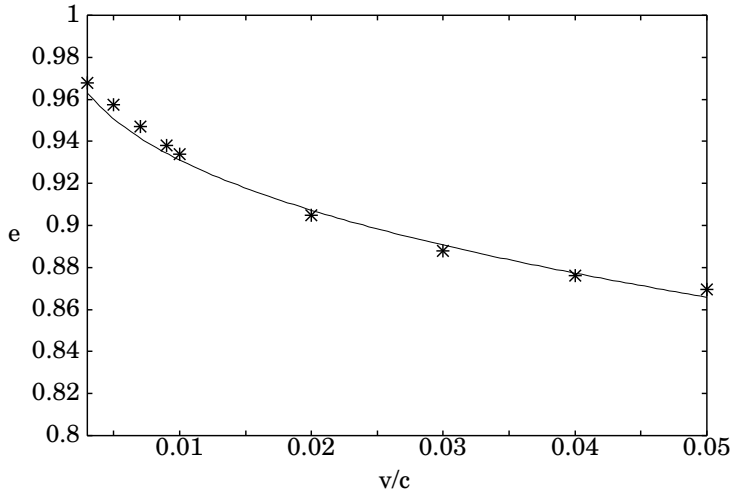

Figure 6.3: The relation between impact velocity and coefficient of restitution.

Chapter 7

General conclusion

In the dissertation, we have carried out two-dimensional simulation of inelastic impact.

At first, in chapter 2, we performed the normal impact of the triangular lattice disk on the structureless wall expressed by an exponential function. In our simulation, COR decreases as the normal impact velocity increases as experimental tendency. The relation between normal impact speed of colliding disk and COR cannot be reproduced by the quasi-static theory which is the standard method to describe low speed impact. However, the relation between the duration and the impact velocity can be well reproduced by the two-dimensional Hertzian contact theory. COR showed the abrupt decrease around the critical impact velocity by the plastic deformation. The critical velocity of the plastic deformation seems to obey a simple linear function of temperature.

In chapter 3, we performed the simulation of the normal impact of an elastic disk and an elastic wall. When the initial velocity is fixed, COR of the disk decreases as the thickness of the wall is thickened as the experimental results by Sondergaard *et al.*.

In chapter 4, we performed the simulation of the oblique impact of an elastic disk and an elastic wall to investigate the relation between the incident angle and the coefficient of tangential restitution. From the comparison between our numerical results and Walton's argument of oblique impact, the maximum value of the coefficient of tangential restitution, β_0, takes a positive value, which means that rotational motion can be generated after an impact. To generate rotational motion, roughness on surfaces of the model is very important. With roughness on surfaces, we can reproduce a realistic rotational motion after collision without any dissipation mechanism.

In chapter 5, we reproduced the experimental setup of the experiment by Louge and Adams[30] and showed the anomalous behavior of COR against the incident angle with the aid of similar model to that in chapter 4. In the case of soft wall, the local deformation on the surface of the wall will make the trajectory of the rebounded disk deflect from the expected direction. This makes COR exceed unity in the large incident angle. The relation between the incident angle and COR can be explained by our phenomenological theory. In addition, it has been confirmed that the coefficient of friction affect the relation between the incident angle and COR. The behavior of the coefficient of friction against the incident angle can be well reproduced by our phenomenological theory.

Appendix A

Walton's collision model

In this appendix, we review the Walton's model of the oblique impact in detail [31, 32, 80, 81]. Here, we restrict our interest to the slip region in oblique impacts.

Figure A.1 depicts a situation of a binary collision of objects 1 and 2. Here, objects 1 and 2 are colliding each other with initial velocities $\mathbf{v}_1$ and $\mathbf{v}_2$ and angular velocities $\boldsymbol{\omega}_1$ and $\boldsymbol{\omega}_2$, respectively. We denote the velocity of the contact point as $\mathbf{v}^{(c)}$, and $\mathbf{v}_n^{(c)}$ and $\mathbf{v}_t^{(c)}$ as $\mathbf{v}_n^{(c)} = \mathbf{v}^{(c)} \cdot \mathbf{n}$ and $\mathbf{v}_t^{(c)} = \mathbf{v}^{(c)} \cdot \mathbf{t}$, respectively. Normal unit vector to the tangential plane $\mathbf{n}$ is

$$\mathbf{n} = \frac{\mathbf{r}_1 - \mathbf{r}_2}{|\mathbf{r}_1 - \mathbf{r}_2|}, \tag{A.1}$$

where $\mathbf{r}_i$ is the vector to the center of particle i ($i = 1, 2$) and tangential unit vector for their contact $\mathbf{t}$ is vertical to $\mathbf{n}$. The angle of incidence γ is defined as the angle between $\mathbf{n}$ and $\mathbf{v}^{(c)}$. For simplicity, we assume that they have same mass m and radius R. The conservation laws for the impulse $\mathbf{P}$ and the angular momentum $-R\mathbf{n} \times \mathbf{P}$ lead to

$$\begin{aligned} \Delta\mathbf{P} &\equiv m\left(\mathbf{v}_1^{'} - \mathbf{v}_1\right) = -m\left(\mathbf{v}_2^{'} - \mathbf{v}_2\right) \\ -\mathbf{n} \times \Delta\mathbf{P} &\equiv \frac{I}{R}\left(\boldsymbol{\omega}_1^{'} - \boldsymbol{\omega}_1\right) = \frac{I}{R}\left(\boldsymbol{\omega}_2^{'} - \boldsymbol{\omega}_2\right), \end{aligned} \tag{A.2}$$

where I is the moment of inertia and $\Delta\mathbf{P}$ is the change of impulse.

Now we calculate the normal and tangential components of the change of impulse, $\Delta\mathbf{P}$, respectively. At first, the relative velocity of the contact point $\mathbf{v}^{(c)}$ is expressed as

$$\mathbf{v}^{(c)} = \mathbf{v}_1 - \mathbf{v}_2 - (R\boldsymbol{\omega}_1 + R\boldsymbol{\omega}_2) \times \mathbf{n}. \tag{A.3}$$

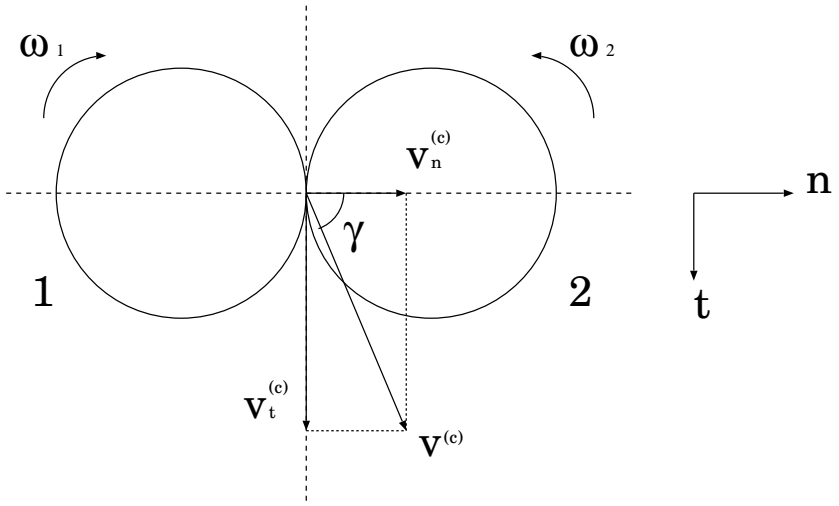

Figure A.1: The schematic figure of binary collision.

Next, we express $\Delta\mathbf{P}$ as the combination of $\mathbf{v}_n^{(c)}$ and $\mathbf{v}_t^{(c)}$. The normal component of the change of impulse can be calculated from (A.2) as

$$\Delta\mathbf{P}_n = -\frac{m}{2}(1+e)\mathbf{v}_n^{(c)}. \tag{A.4}$$

Here, we used the definition of normal COR, $\mathbf{v}_n^{(c)'} = -e\mathbf{v}_n^{(c)}$. We assume that the tangential change of impulse satisfies

$$\left|\Delta\mathbf{P}_t^{(c)}\right| = \mu_0 \left|\Delta\mathbf{P}_n^{(c)}\right|, \tag{A.5}$$

where μ_0 in the coefficient of friction for large γ impacts. This assumption leads to

$$\Delta\mathbf{P}_t = \left|\Delta\mathbf{P}_{(t)}\right|\mathbf{t} = -\mu_0\frac{m}{2}(1+e)v^{(c)}\cos\gamma\mathbf{t}. \tag{A.6}$$

Here, we used $\left|\mathbf{v}_n^{(c)}\right| = v^{(c)}\cos\gamma$. Using the definition of $\mathbf{t}$, $\mathbf{t} = \mathbf{v}_t^{(c)}/\left|\mathbf{v}_t^{(c)}\right| = \mathbf{v}_t^{(c)}/v^{(c)}\sin\gamma$, (A.6) becomes

$$\Delta\mathbf{P}_{(t)} = -\frac{m}{2}\mu_0(1+e)\cot\gamma\mathbf{v}_t^{(c)}. \tag{A.7}$$

Therefore, from (A.4) and (A.7), $\Delta\mathbf{P}$ can be expressed as

$$\Delta\mathbf{P} = -\frac{m}{2}(1+e)\mathbf{v}_n^{(c)} - \frac{m}{2}\mu_0(1+e)\cot\gamma\mathbf{v}_t^{(c)}. \tag{A.8}$$

From (A.8), one can express the rebound velocity of contact point $\mathbf{v}^{(c)'}$ as the combination of $\mathbf{v}_n^{(c)}$ and $\mathbf{v}_t^{(c)}$. $\mathbf{v}^{(c)'}$ can be expressed from (A.2) and (A.3) as

$$\begin{aligned}\mathbf{v}^{(c)'} &= \mathbf{v}^{(c)} + \frac{2}{m}\Delta\mathbf{P} + \frac{2R^2}{I}\Delta\mathbf{P}_t \\ &= -e\mathbf{v}_n^{(c)} - \left(-1 + \mu_0(1+e)\cot\gamma\left(1+\frac{mR^2}{I}\right)\right)\mathbf{v}_t^{(c)}, \end{aligned}\tag{A.9}$$

where we used (A.7) and (A.8). From the definition of β, $\mathbf{v}_t^{(c)'} = -\beta\mathbf{v}_t^{(c)}$, we obtain

$$\beta = -1 + \mu_0(1+e)\cot\gamma\left(1+\frac{mR^2}{I}\right) \tag{A.10}$$

for slip region of oblique impacts.

Appendix B

The Theoretical description of the oblique impact

B.1 The equation of motion

In this appendix, we review and rewrite the theory of oblique impacts[29, 27, 28] for our investigation. Let us consider a collision between a disk with the radius R and a rectangle with the hight $2R$ and the width $8R$ at the contact point denoted as C. In the subsequent discussion, the disk and the wall are assumed to contact at C in the total collision process though they contact each other on a line in practice. When comparing the theory with our numerical results, we average all positions of particles on the contact line to define the position of the contact point C.

We assume that the first contact begins at the time $t = 0$ (Fig.B.1) and compression and restitution periods terminate at $t = t_c$ and $t = t_f$, respectively. In the total collision process, we define relative velocity and displacement of a disk at the contact point C to a rectangle as v_i and u_i $(i = x, z)$, respectively. A disk and a rectangle have masses M and $M^{'}$ and their radii of gyration $\hat{k}_r = R/\sqrt{2}$ and $\hat{k}_r^{'} = R\sqrt{17/3}$ around their centers of mass, respectively. The prime denotes parameters for the rectangle. The position of the contact point C is denoted as $(r_x, r_z) = (0, -R)$ or $(r_x^{'}, r_z^{'}) = (0, R)$ which are measured from the centers of mass of each colliding body. We assume that both normal and tangential elements of the compliance are proportional to the compression. We also introduce the normal stiffness during compression κ, and the tangential stiffness during compression κ/η^2 for the disk. The equation of motion of the displacements, thus,

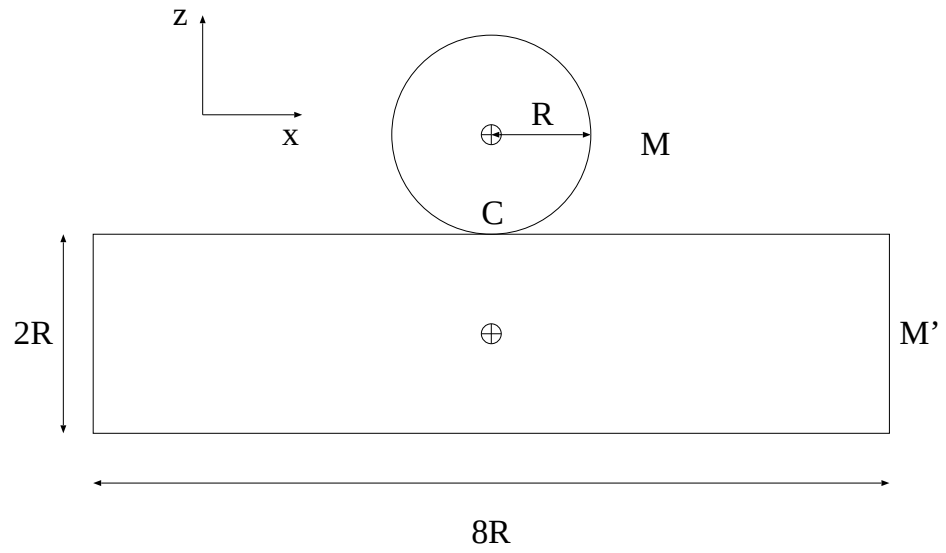

Figure B.1: The schematic figure of the disk and the wall. A cross in a circle represents a center of mass of each body.

becomes

$$\begin{pmatrix} \ddot{u}_x \\ \ddot{u}_z \end{pmatrix} = -m^{-1}\kappa \begin{bmatrix} \beta_x \eta^{-2} & 0 \\ 0 & \beta_z \end{bmatrix} \begin{pmatrix} u_x \\ u_z \end{pmatrix}, \tag{B.1}$$

where $\ddot{u}_x = d^2u_x/dt^2$, $m = MM^{'}/(M + M^{'})$, and

$$\beta_x = 1 + \frac{mr_z^2}{M\hat{k}_r^2} + \frac{mr_z^{'2}}{M^{'}\hat{k^{'}}_r^2}, \quad \beta_z = 1 + \frac{mr_x^2}{M\hat{k}_r^2} + \frac{mr_x^{'2}}{M^{'}\hat{k^{'}}_r^2}. \tag{B.2}$$

In our situation, β_x and β_z can be calculated as $\beta_x \simeq 3.02$ and $\beta_z = 1$.

Equation of motion (B.1) has two characteristic frequencies, Ω and ω, which are expressed as

$$\Omega \equiv \sqrt{\frac{\beta_z \kappa}{m}}, \quad \omega \equiv \sqrt{\frac{\beta_x \kappa}{\eta^2 m}} = \frac{1}{\eta}\sqrt{\frac{\beta_x}{\beta_z}}\Omega \tag{B.3}$$

in the normal and tangential direction to the wall, respectively. One can also express them using t_c, the time when the normal velocity of compression becomes 0 ($\dot{u_z}(t_c) = 0$), as $\Omega = \pi/2t_c$ and $\omega = (\pi/2\eta t_c)\sqrt{\beta_x/\beta_z}$. According to

Johnson[25], stiffnesses in the normal and tangential direction, κ and κ/η^2, can be expressed using Young's modulus E, the radius of punch a, and Poisson's ratio ν as

$$\kappa = \frac{Ea}{1-\nu^2}, \quad \kappa/\eta^2 = \frac{2Ea}{(2-\nu)(1+\nu)}. \tag{B.4}$$

Thus, η can be expressed only by the Poisson's ratio,

$$\eta = \sqrt{\frac{2-\nu}{2(1-\nu)}}. \tag{B.5}$$

Here we define the coefficient of restitution for subsequent discussion. The coefficient of restitution is defined as

$$e_* \equiv \frac{p_z(t_f) - p_z(t_c)}{p_z(t_c)}, \tag{B.6}$$

where $p_z(t)$ is the normal impulse. We can show that e_* is equivalent to the conventional normal coefficient of restitution e. $v_z(t)$ is the normal velocity, and v_0 is the initial normal velocity. This leads to $p_z(t_f) = (1+e_*)p_z(t_c)$ and $t_f = (1+e_*)t_c$. In the later discussion, we assume that the effect of the coefficient of restitution e_* is obtained by changing the stiffness of the normal compliant element from κ to κ/e_*^2 at $t = t_c$. Thus, from Eq.(B.3), the normal frequency increases from Ω to Ω/e_* at $t = t_c$.

B.2 Velocity and force of the contact point

To obtain the relation between the tangential coefficient of restitution β and the angle of incidence γ, we take into account that the motion of the disk during collision depends on the angle of incidence. According as γ increases, the motion of the disk during collision is classified into three regions: (i) The disk sticks initially and begins to slip at $t = t_1$. (ii) The disk slips until $t = t_2$ and sticks for $t_2 < t < t_3$ and then it slips again until $t = t_f$. (iii) The disk slips during collision. We need to calculate the initial and terminal velocities of the contact point of the disk in each region. For the initial and terminal velocities of the disk, we have to calculate t_1, t_2, and t_3 from the force acting on the contact point. In this section, we show how to obtain normal and tangential components of velocity and force and how to calculate t_1 in the region (i).

Table B.1: Normal displacement, velocity, force, and impulse

Quantity	Compression $(0 \le t \le t_c)$	Restitution $(t_c \le t \le t_f)$
Displacement	$u_z(t) = -\Omega^{-1} v_z(0) \sin \Omega t$	$u_z(t) = -e_*^2 \Omega^{-1} v_z(0) \sin\left(\frac{\Omega t}{e_*} + \frac{\pi}{2}\left(1 - e_*^{-1}\right)\right)$
Velocity	$v_z(t) = v_z(0) \cos \Omega t$	$v_z(t) = e_* v_z(0) \cos\left(\frac{\Omega t}{e_*} + \frac{\pi}{2}\left(1 - e_*^{-1}\right)\right)$
Force	$F_z(t) = -\frac{m\Omega v_z(0)}{\beta_z} \sin \Omega t \ge 0$	$F_z(t) = -\frac{m\Omega v_z(0)}{\beta_z} \sin\left(\frac{\Omega t}{e_*} + \frac{\pi}{2}\left(1 - e_*^{-1}\right)\right) \ge 0$
Impulse	$p_z(t) = -\frac{m v_z(0)}{\beta_z}\left(1 - \cos \Omega t\right)$	$p_z(t) = -\frac{m v_z(0)}{\beta_z}\left(1 - e_* \cos\left(\frac{\Omega t}{e_*} + \frac{\pi}{2}\left(1 - e_*^{-1}\right)\right)\right)$

B.2.1 Normal components of velocity and force

By solving Eq.(B.1), we can obtain normal components of velocity and force. Assuming $v_z(t) + \dot{u}_z(z) = 0$ during contact, we obtain

$$v_z(t) = \begin{cases} v_z(0) \cos \Omega t & 0 \le t \le t_c \\ e_* v_z(0) \cos(\frac{\Omega t}{e_*} + \frac{\pi}{2}(1 - e_*^{-1})) & t_c \le t \le t_f. \end{cases} \tag{B.7}$$

Assuming that the normal frequencies during restitution is Ω/e_* and the initial conditions $v_z(t_c) = 0$ and $v_z(t_f) = -e_* v_z(0)$, we reach the exact form of solution during restitution period. (B.7) is continuous at $t = t_c$. By differentiating these expressions, we also obtain the displacement $u_z(t)$, the force $F_z(t)$, and the impulse $p_z(t)$ as described in Table B.1.

B.2.2 Tangential components of velocity and force

Let us consider the region (ii). We assume that a disk slips on the surface of a rectangle during collision and starts sticking at $t = t_2$. At $t = t_2$, assuming Coulomb's law of friction, the relation between F_x and F_z becomes $|F_x| < \mu F_z$, where μ is the coefficient of friction. We calculate the expressions for tangential components for sticking and slipping separately.

While a disk slips on the surface of a rectangle, the relation between F_x and F_z is $|F_x|/F_z = \mu$ and the tangential velocity is changed by a impulse arising from contact force. Thus, the change of velocity can be described as

$$\begin{pmatrix} dv_x/dp_z \\ dv_z/dp_z \end{pmatrix} = m^{-1} \begin{bmatrix} \beta_x & 0 \\ 0 & \beta_z \end{bmatrix} \begin{pmatrix} -\mu sgn(v_x + \dot{u}_x) \\ 1 \end{pmatrix} \qquad t < t_2, \tag{B.8}$$

where $sgn(x) = +1$ for $x > 0$ and $sgn(x) = -1$ for $x < 0$.

When a disk starts sticking at $t = t_2$, the tangential oscillation starts with frequency ω. We assume $v_x(t) + \dot{u}_x(t) = 0$. By solving the equation of $u_x(t)$, we can obtain the tangential components of displacement, velocity, and contact force as

$$\begin{aligned} u_x(t) &= u_x(t_2)\cos\omega(t-t_2) - \omega^{-1}v_x(t_2)\sin\omega(t-t_2) \\ v_x(t) &= \omega u_x(t_2)\sin\omega(t-t_2) + v_x(t_2)\cos\omega(t-t_2) \\ F_x(t) &= m\beta_x^{-1}\omega^2 u_x(t_2)\cos\omega(t-t_2) - m\beta_x^{-1}\omega v_x(t_2)\sin\omega(t-t_2) \qquad t \geq t_2. \end{aligned} \tag{B.9}$$

B.2.3 Obtaining the transition time, t_1

Let us consider the region (i). From (B.9) with the condition $u_x(0) = 0$ and $F_z(t)$ described in the Table B.1, t_1 can be obtained by solving the equation

$$\frac{|F_x(t_1)|}{\mu F_z(t_1)} = \begin{cases} \dfrac{1}{\eta^2}\dfrac{v_x(0)}{\mu v_z(0)}\dfrac{\Omega}{\omega}\dfrac{\sin\omega t_1}{\sin\Omega t_1} = 1 & 0 \leq t_1 < t_c \\ \dfrac{1}{\eta^2}\dfrac{v_x(0)}{\mu v_z(0)}\dfrac{\Omega}{\omega}\dfrac{\sin\omega t_1}{\sin(\frac{\Omega t_1}{e_*} + \frac{\pi}{2}(1-e_*^{-1}))} = 1 & t_c \leq t_1 < t_f. \end{cases} \tag{B.10}$$

Solving these equation numerically, we obtain t_1. It should be noted that there are two conditions if t_1 is greater or smaller than t_c.

The process of initial stick takes place if $t_1 > 0$, *i.e.* if in the limit as $t_1 \to 0$ the force ratio between the tangential and normal component is smaller than μ. This requires

$$\frac{v_x(0)}{v_z(0)} < \mu\eta^2. \tag{B.11}$$

B.3 Three regimes of the angle of incidence

Here, we divide all region of the angle of incidence into three regimes and calculate the tangential component of terminal velocity of collision for each regime.

(i) **Small angle of incidence:** $v_x(0)/v_z(0) < \mu\eta^2$

In this regime, initial stick continues until $t = t_1$ and slip terminates at $t = t_f$. At time t_1, the tangential component of the relative velocity is $v_x(t_1) =$

$v_x(0)\cos\omega t_1$. From Eq.(B.8), the terminal tangential velocity can be expressed as

$$v_x(t_f) = v_x(0)\cos\omega t_1 - \frac{\mu\beta_x}{m}[p_z(t_f) - p_z(t_1)], \tag{B.12}$$

where $p_z(t_f) - p_z(t_1)$ can be expressed as

$$p_z(t_f) - p_z(t_1) = -m\frac{v_z(0)}{\beta_z}e_*\{1 + \cos(\frac{\Omega t_1}{e_*} + \frac{\pi}{2}(1 - e_*^{-1}))\} \tag{B.13}$$

from Table B.1. Dividing Eq.(B.12) by $-v_x(0)$ leads to

$$\beta = -\cos\omega t_1(\gamma) - \mu\frac{\beta_x}{\beta_z}e_*\left[1 + \cos\left(\frac{\Omega t_1(\gamma)}{e_*} + \frac{\pi}{2}(1 - e_*^{-1})\right)\right]\cot\gamma, \tag{B.14}$$

where β is $-v_x(t_f)/v_x(0)$ and $\cot\gamma$ is $v_z(0)/v_x(0)$.

(ii) **Intermediate angle of incidence:** $\mu\eta^2 < v_x(0)/v_z(0) < \mu(1+e_*)\beta_x/\beta_z$

In this regime, the disk initially slips and begins to stick at $t = t_2$. After the period of sticking, the disk begins to slip again at $t = t_3$. In the period $t < t_2$, the tangential component of relative velocity is written as

$$v_x(t) = v_x(0) - \frac{\mu\beta_x}{m}p_z(t). \tag{B.15}$$

Here let us calculate t_2 and t_3. At $t = t_2$, subsequent sliding and stick give the same rate of change for the tangential force:

$$\lim_{\epsilon\to 0}\left|\frac{dF_x(t_2+\epsilon)}{d\epsilon}\right| = \lim_{\epsilon\to 0}\mu\frac{dF_z(t_2+\epsilon)}{d\epsilon}. \tag{B.16}$$

This is the condition which determines t_2. To simplify this condition, we need to obtain the exact forms of $dF_x(t)/dt$ and $dF_z(t)/dt$.

For tangential components of force, if one differentiate Eq.(B.9) by t, we obtain

$$\frac{dF_x(t)}{dt} = \frac{m\omega^3 u_x(t_2)}{\beta_x}\sin\omega(t-t_2) - \frac{m\omega^2 v_x(t_2)}{\beta_x}\cos\omega(t-t_2) \qquad t > t_2. \tag{B.17}$$

Here, $v_x(t)$ is represented by Eq.(B.15) and with the aid of Table B.1, and $u_x(t)$ is obtained from $v_x(t) + \dot{u}_x(t) = 0$. Thus, the explicit expressions are

$$\begin{aligned} v_x(t_2) &= \begin{cases} v_x(0) - \mu\frac{\beta_x}{\beta_z} v_z(0)[1 - \cos\Omega t_2] & t_2 \le t_c \\ v_x(0) - \mu\frac{\beta_x}{\beta_z} v_z(0)\left[1 - \cos\left(\frac{\Omega t_2}{e_*} + \frac{\pi}{2}(1 - e_*^{-1})\right)\right] & t_2 > t_c \end{cases} \\ u_x(t_2) &= \begin{cases} \mu\frac{\beta_x \Omega v_z(0)}{\beta_z \omega^2}\sin\Omega t_2, & t_2 \le t_c \\ \mu\frac{\beta_x \Omega v_z(0)}{\beta_z \omega^2}\sin\left(\frac{\Omega t_2}{e_*} + \frac{\pi}{2}(1 - e_*^{-1})\right) & t_2 > t_c \end{cases} \end{aligned} \tag{B.18}$$

For normal components of force, by differentiating the expressions of normal components in Table B.1, we can obtain

$$\frac{dF_z(t_2)}{dt} = \begin{cases} -\beta_z^{-1}\Omega^2 m v_z(0)\cos\Omega t_2 & t_2 \le t_c \\ -\frac{\Omega^2 m v_z(0)}{\beta_z e_*}\cos(\frac{\Omega t_2}{e_*} + \frac{\pi}{2}(1 - e_*^{-1})) & t_2 \ge t_c \end{cases} \tag{B.19}$$

From (B.17), (B.18), and (B.19), Eq.(B.16) leads to

$$\Omega t_2 = \arccos\left(\frac{v_x(0)/\mu v_z(0) - \beta_x/\beta_z}{\eta^2 - \beta_x/\beta_z}\right) \qquad \frac{v_x(0)}{v_z(0)} \le \mu\frac{\beta_x}{\beta_z} \tag{B.20}$$

$$\frac{\Omega t_2}{e_*} = -\frac{\pi}{2}(1 - e_*^{-1}) + \arccos\left(\frac{v_x(0)/\mu v_z(0) - \beta_x/\beta_z}{\eta^2 e_*^{-1} - e_*\beta_x/\beta_z}\right) \qquad \frac{v_x(0)}{v_z(0)} > \mu\frac{\beta_x}{\beta_z}$$

In the period $t_2 < t < t_3$, the velocity and the force are expressed as Eq.(B.9). This period of stick terminates and slip begins at time $t = t_3$. t_3 can be determined by the condition $|F_x|/F_z = \mu$. From Eq.(B.9) and Table B.1, this condition leads to

$$\left|\frac{\Omega u_x(t_2)}{\mu v_z(0)}\cos\omega(t_3 - t_2) - \frac{\Omega v_x(t_2)}{\omega\mu v_z(0)}\sin\omega(t_3 - t_2)\right| = \eta^2\sin\left[\frac{\Omega t_3}{e_*} + \frac{\pi}{2}(1 - e_*^{-1})\right]. \tag{B.21}$$

Solving this equation numerically, we obtain t_3. The final tangential velocity is expressed as

$$v_x(t_f) = v_x(t_3) - \mu\beta_x m^{-1}[p_z(t_f) - p_z(t_3)], \tag{B.22}$$

where $p_z(t)$ is expressed in Table B.1. Dividing (B.22) by $-v_x(0)$, we obtain

$$\begin{aligned} \beta = &-\cos\omega(t_3 - t_2) - \mu\frac{\beta_x}{\beta_z}[\cos\omega(t_3 - t_2) - \cos\Omega t_2\cos\omega(t_3 - t_2) \\ &+ \frac{\Omega}{\omega}\sin\Omega t_2\sin\omega(t_3 - t_2) + e + \cos\Omega t_3]\cot\gamma. \end{aligned} \tag{B.23}$$

(iii) **Large angle of incidence:** $v_x(0)/v_z(0) > \mu(1+e_*)\beta_x/\beta_z$

In this regime, slip does not cease before separation: $t_2 > t_f$. At separation, the tangential velocity $v_x(t_f)$ if as follows:

$$v_x(t_f) = v_x(0) + \mu\beta_x m^{-1}(1+e_*)p_z(t_c), \tag{B.24}$$

where $p_z(t_c) = -mv_z(0)/\beta_z$. Thus, dividing (B.24) by $-v_x(0)$, we obtain

$$\beta = -1 + \mu\frac{\beta_x}{\beta_z}(1+e_*)\cot\gamma. \tag{B.25}$$

Appendix C

Poisson's ratio for a square lattice system with next-nearest neighbor interaction

In this appendix, we derive the relation between elastic constants in continuum limit and spring constants of a two-dimensional square lattice with nearest neighbor coupling k_1 and next-nearest neighbor coupling k_2(Fig. 4.4). The elastic tensor C_{ijkl} for the two dimensional square lattice is represented as

$$C_{xxxx} = C_{yyyy} = k_1 + k_2, \tag{C.1}$$

$$C_{xxyy} = C_{yyxx} = C_{xyyx} = C_{yxxy} = C_{xyxy} = C_{yxyx} = k_2, \tag{C.2}$$

and the other coefficients are zero[82].

Using the elastic tensor C_{ijkl} and the strain tensor u_{ij} and u_{kl}, The free energy of the system U is represented as

$$U = \frac{1}{2} C_{ijkl} u_{ij} u_{kl}. \tag{C.3}$$

Thus, we obtain the stress tensor σ_{ij} as

$$\sigma_{ij} = \frac{\partial U}{\partial u_{ij}} = C_{ijkl} u_{kl}. \tag{C.4}$$

Now we introduce the unit vector $\mathbf{n}$ in the axial direction of the rod. When we pull both sides of the rod with the pressure p_r, the relation

$$\sigma_{ik} = p_r n_i n_k \tag{C.5}$$

holds.

From eqs (C.1), (C.2) and (C.5), the explicit expressions of the stress tensors become

$$\sigma_{xx} = C_{xxxx}u_{xx} + C_{xxyy}u_{yy} = (k_1 + k_2)u_{xx} + k_2 u_{yy} = p_r n_x^2 \quad \text{(C.6)}$$

$$\sigma_{yy} = C_{yyxx}u_{xx} + C_{yyyy}u_{yy} = k_2 u_{xx} + (k_1 + k_2)u_{yy} = p_r n_y^2 \quad \text{(C.7)}$$

$$\sigma_{xy} = C_{xyxy}u_{xy} + C_{xyyx}u_{yx} = 2k_2 u_{xy} = p_r n_x n_y. \quad \text{(C.8)}$$

From these equations, we obtain the expressions of the strain tensors,

$$u_{xx} = p_r \frac{(k_1 + k_2)n_x^2 - k_2 n_y^2}{k_1(k_1 + 2k_2)} \quad \text{(C.9)}$$

$$u_{yy} = p_r \frac{(k_1 + k_2)n_y^2 - k_2 n_x^2}{k_1(k_1 + 2k_2)} \quad \text{(C.10)}$$

$$u_{xy} = p_r \frac{n_x n_y}{2k_2}. \quad \text{(C.11)}$$

The strain in the direction of $\mathbf{n}$ is expressed as $u = u_{ik}n_i n_k$. Thus, we have

$$u = u_{xx}n_x^2 + 2u_{xy}n_x n_y + u_{yy}n_y^2 \quad \text{(C.12)}$$

$$= \left\{ \frac{k_1 + k_2}{k_1(k_1 + 2k_2)} + \frac{k_1 - 2k_2}{k_1 k_2} n_x^2 n_y^2 \right\} p_r. \quad \text{(C.13)}$$

Therefore we obtain Young's modulus as

$$\frac{1}{E} = \frac{k_1 + k_2}{k_1(k_1 + 2k_2)} + \frac{k_1 - 2k_2}{k_1 k_2} n_x^2 n_y^2. \quad \text{(C.14)}$$

On the other hand, the Poisson's ratio ν is defined as the ratio of the normal strain to the vertical strain. The latter is described as

$$u_t = u_{xx}n_y^2 - 2u_{xy}n_x n_y + u_{yy}n_x^2 \quad \text{(C.15)}$$

$$= \left\{ \frac{2(k_1 + 2k_2)n_x^2 n_y^2 - k_2}{k_1(k_1 + 2k_2)} - \frac{n_x^2 n_y^2}{k_2} \right\} p_r. \quad \text{(C.16)}$$

Thus, Poisson's ratio is given by

$$\nu = \frac{k_2^2 + (k_1^2 - 4k_2^2)n_x^2 n_y^2}{k_2(k_1 + k_2) + (k_1^2 - 4k_2^2)n_x^2 n_y^2}. \quad \text{(C.17)}$$

Appendix D

Contact of a hard disk on an elastic half-space

In this appendix, we briefly explain the derivation of Eq.(5.3) following the text book of Hills[51].

Let us consider two cylinders with radii R_1 and R_2 pressed together, which may be treated by two-dimensional Hertzian contact theory. If we express the pressure distribution as $p(x)$, the macroscopic deformation h can be described by following equation[51]:

$$\frac{1}{A_Y}\frac{\partial h}{\partial x} = \frac{1}{\pi}\int \frac{p(\xi)d\xi}{x-\xi} - \beta_Y \mu p(x), \tag{D.1}$$

where

$$A_Y = 2\left(\frac{1-\nu_1^2}{E_1} + \frac{1-\nu_2^2}{E_2}\right), \tag{D.2}$$

$$\beta_Y = \frac{1}{2}\frac{(1+\nu_1)(1-2\nu_1)/E_1 - (1+\nu_2)(1-2\nu_2)/E_2}{(1-\nu_1^2)/E_1 + (1-\nu_2^2)/E_2}. \tag{D.3}$$

The second term of the right hand side of Eq.(D.1) assumes Coulomb's friction law by introducing Coulomb's friction coefficient μ. The integral of Eq.(D.1) is carried out over the contact area. External normal force P is defined by

$$P = -\int p(\xi)d\xi. \tag{D.4}$$

Assuming the load is sufficiently small for the contact area $2a$, the relative normal approach of cylinders within the contact can be approximated by the parabora as

$$h(x) = C - k_c(x - x_c)^2/2, \tag{D.5}$$

where C is a maximum approach, k_c is the relative curvature given by $k_c = 1/R_1 + 1/R_2$, and x_c is the x coordinate of the top of the cylinder. If we assume the body 1 as a rigid disk by letting E_1 go to infinity and the body 2 as a elastic half-space by letting R_2 go to infinity and replacing ν_2 by ν, β_Y and k_c become

$$\beta_Y = \frac{1 - 2\nu}{2\,(1 - \nu)} \quad \text{and} \quad k_c = \frac{1}{R_1}. \tag{D.6}$$

From Eq.(D.1) and (D.5), we can obtain

$$\frac{1}{\pi}\int_{-a}^{a} \frac{p(\xi)d\xi}{x - \xi} + \beta_Y \mu p(x) = \frac{-k_c(x - x_c)}{A_Y}. \tag{D.7}$$

By introducing scaling patameters, $x = as$ and $\xi = ar$, Eq. (D.7) becomes

$$\frac{1}{\pi}\int_{-1}^{1} \frac{p(r)dr}{r - s} - \beta_Y \mu p(s) = \frac{-k_c x_c + k_c a s}{A_Y}. \tag{D.8}$$

From the general solution of a Cauchy singular integral equation of the second kind[51], we obtain

$$p(s) = -\left(\frac{k_c a}{A_Y} \sin m\pi (1 - s)^m (1 + s)^{1-m}\right), \tag{D.9}$$

$$\text{where} \quad \tan(m\pi) = \frac{1}{\beta_Y \mu} \quad 0 < m < 1, \tag{D.10}$$

which is accompnied by the consistency condition,

$$\int_{-1}^{1} \frac{(s - x_c^*)ds}{(1 - s)^m (1 + s)^{1-m}} = 0, \tag{D.11}$$

where $x_c^* = x_c/a$. Eq.(D.11) yields

$$x_c^* = 2m - 1. \tag{D.12}$$

By substituting $x_a = -a$ and $l_c = 2a$ into Eq.(D.12), we can obtain Eq.(5.3). External normal force P is calculated as

$$\begin{aligned} P &= -\int_{-1}^{1} p(s)ds \\ &= \frac{2\pi k_c a^2 m(1-m)}{A_Y}. \end{aligned} \tag{D.13}$$

From Eq.(D.9) and (D.13), we obtain

$$p(s) = -\frac{P \sin m\pi}{2\pi a m(1-m)}(1-s)^m(1+s)^{1-m}. \tag{D.14}$$

In the case of $m = 1/2(\mu = 0)$, which means that there is no external shear force, Eq.(D.14) is identical to the result from two-dimensional Hertzian contact theory[49].

Appendix E

The Chronological table of impact studies

Year	Literature	Contents
1600		
87	I. Newton, *Principia*	Introduction of COR
1800		
34	E. Hodgikinson, Brit. Assoc. Report, **4**, 535	COR of various materials
82	H. Hertz, J. Reine Angew. Math, **92**, 156	Contact theory
92	A. E. H. Love, *A Treatise on the Mathematical Theory of Elasticity*(1st ed.)	Impact theory of Hertz(A text book of theory of elasticity)
1900		
00	J. H. Vincent, Proc. Cambridge, Phil. Soc. **10**, 332	COR as a function of impact velocity
06	O. M. Rayleigh, Philos. Mag. Ser. 6 **11**, 283	Vibrational analysis
18	C. V. Raman, Phys. Rev. **12**, 442	Photographic study of COR's dependency on impact velocity
34	S. P. Timoshenko and J. N. Goodier, *Theory of Elasticity*(1st ed.)	Impact theory of Hertz(A text book of theory of elasticity)
40	R. D. Mindlin, J. Appl. Mech., **16**, 259	Tangential contact force

Year	Literature	Contents
53	L. D. Landau and E. M. Lifshitz, *Theory of Elasticity*(1st ed.)	Impact theory of Hertz(A text book of theory of elasticity)
60	W. Goldsmith, *Impact: the theory and physical behavior of colliding solids* (London:Arnold)	Textbook of impact
76	N. Maw, J. R. Barber, and J. N. Fawcett, Wear, **38**, 101	Theory of oblique impact
81	N. Maw, J. R. Barber, and J. N. Fawcett, J. Lub. Tech, **103**, 74	Theory and experiment of oblique impact
84	F. G. Bridges, A. Hatzes, and D. N. C. Lin, Nature, **309**, 333	Impact experiment of ice spheres
86	K. L. Johnson, *Contact Mechanics* (Cambridge:Cambridge Univ. Press)	Text book of contact mechanics
87	G. Kuwabara and K. Kono, Jpn. J. Appl. Phys., **26**, 1230	Quasi-static theory
95	J. Schäfer, S. Dippel, and D. E. Wolf, Phys. Rev. E, **52**, 4442	Comparison of force schemes used in simulation
96	N. Brilliantov, F. Spahn, J.-M. Hertzsch, and T. Pöschel, Phys. Rev. E, **53**, 5382	Quasi-static theory
97	W. A. Morgado and I. Oppenheim, Phys. Rev. E, **55**, 1940	Quasi-static theory
98	T. Schwager and T. Pöschel, Phys. Rev. E, **57**, 650	Quasi-static theory
99	R. Ramírez, T. Pöschel, N. V. Brilliantov and T. Schwager, Phys. Rev. E, **60**, 4465	Quasi-static theory
2000		
00	W. J. Stronge, Impact Mechanics (Cambridge:Cambridge Univ. Press)	Systematic text book of impact
03	M. Y. Louge and M. E. Adams, Phys. Rev. E, **65**, 021303	COR exceeding 1 experimentally

Bibliography

[1] I. Newton. *Philoshophiae naturalis Principia mathematica*. W. Dawason and Sons, London, 1962.

[2] F. G. Bridges, A. Hatzes, and D.N.C. Lin. Structure, stability and evolution of saturn's rings. *Nature*, 309:333–335, 1984.

[3] K. D. Supulver, F. G. Bridges, and D. N. C. Lin. The coefficient of restitution of ice particles in glancing collisions: Experimental results for unfrosted surfaces. *ICARUS*, 113:188–199, 1995.

[4] L. Labous, A. D. Rosato, and R. N. Dave. Measurements of collisional properties of spheres using high-speed video analysis. *Phys. Rev. E*, 56:5717–5725, 1997.

[5] S. F. Foerster, M. Y. Louge, H. Chang, and K. Allia. Measurements of the collision properties of small spheres. *Phys. Fluids*, 6:1108–1115, 1994.

[6] A. Lorentz, C. Tuozzolo, and M. Y. Louge. Measurements of impact properties of small nearly spherical particles. *Exp. Mech.*, 37:292–298, 1997.

[7] D. A. Gorham and A. H. Kharaz. The measurement of particle rebound characteristics. *Powder Technology*, 112:193–202, 2000.

[8] E. Hodgikinson. On the collision of imperfectly elastic bodies. *Brit. Assoc. Report*, 4:534–543, 1834.

[9] C. V. Raman. The photographic study of impact at minimal velocities. *Phys. Rev.*, 12:442–448, 1918.

[10] J. H. Vincent. Experiments on impact. *Proc. Cambridge, Phil. Soc.*, 10:332–357, 1900.

[11] H. Minamoto and S. Takezono. Elastic impact of two equivalent spheres. *Trans. Jpn. Soc. Mech. Eng.(in Japanese)*, 69:1231–1237, 2003.

[12] Y. Tanaka, Y. Yamazaki, and K. Okumura. Bouncing gel balls: impact of soft gels onto rigid surface. *Europhys. Lett.*, 63(1):146–152, 2003.

[13] E. Falcon, C Laroche, S. Fauve, and C. Coste. Behavior of one inelastic ball bouncing repeatedly off the ground. *Eur. Phys. J. B*, 3:45–57, 1998.

[14] W. Goldsmith. *Impact: The Theory and Physical Behavior of Colliding Solids*. Edward Arnold Publ., London, 1960.

[15] R. Sondergaard, K. Chaney, and C. E. Brennen. Measurements of solid spheres bouncing off flat plates. *Trans. of the ASME, J. Appl. Mech*, 57:694–699, 1990.

[16] F. P. Bowden and D. Tabor. *The Friction and Lubrication of Solids*. Oxford, 1954.

[17] D. Tabor. *The Hardness of Metals*. Oxford University Press., Oxford, 1951.

[18] P. A. Cundall and O. D. L. Strack. A discrete numerical model for granular assemblies. *Géotechnique*, 29:47–65, 1979.

[19] L. P. Kadanoff. Built upon sand: Theoretical ideas inspired by granular flows. *Rev. Mod. Phys.*, 71:435–444, 1999.

[20] P. G. de Gennes. Granular matter: a tentative view. *Rev. Mod. Phys.*, 71:S374–S382, 1999.

[21] H. M. Jaeger and S. R. Nagel. *Science*, 255:1523, 1992.

[22] H. M. Jaeger, S. R. Nagel, and R. P. Behringer. Granular solids, liquids, and gases. *Rev. Mod. Phys.*, 68:1259–1273, 1996.

[23] H. Hayakawa. *Mechanics for the System of Dissipatve Particles (San-itsu Ryuushikei no Rikigaku, in Japanese)*. Iwanami, Tokyo, 2003.

[24] W. Johnson. *Impact Strength of Materials*. Edward Arnold, London, 1972.

[25] K. L. Johnson. *Contact Mechanics*. Cambridge University Press, Cambridge, 1985.

[26] G. Kuwabara and K. Kono. Restitution coefficient in a collision between two spheres. *Jpn. J. Appl. Phys.*, 26:1230–1233, 1987.

[27] N. Maw, J. R. Barber, and J. N. Fawcett. The oblique impact of elastic spheres. *Wear*, 38:101–114, 1976.

[28] N. Maw, J. R. Barber, and J. N. Fawcett. The role of elastic tangential compliance in oblique impact. *J. Lub. Tech*, 103:74–80, 1981.

[29] W. J. Stronge. *Impact Mechanics*. Cambridge University Press, Cambridge, 2000.

[30] M. Y. Louge and M. E. Adams. Anomalous behavior of normal kinematic restitution in the oblique impacts of a hard sphere on an elastoplastic plate. *Phys. Rev. E*, 65:021303–1–021303–6, 2002.

[31] O. R. Walton and R. L. Braun. Viscosity, granular-temerature, and stress calculations for shearing assemblies of inelastic, fritional disks. *J. Rheol.*, 30:949–980, 1986.

[32] O. R. Walton. Numerical simulation of inelastic, frictional particle-particle interactions. In M. C. Roco, editor, *Particulate Two Phase Flow*, pages 884–907, Boston, 1992. Butterworth-Heinemann.

[33] N. Brilliantov, F. Spahn, J.-M. Hertzsch, and T. Pöschel. Model for collisions in granular gases. *Phys. Rev. E*, 53:5382–5392, 1996.

[34] W. A. Morgado and I. Oppenheim. Energy dissipation for quasielastic granular particle collisions. *Phys. Rev. E*, 55:1940–1945, 1997.

[35] T. Schwager and T. Pöschel. Coefficient of normal restitution of viscous particles and cooling rate of granular gases. *Phys. Rev. E*, 57:650–654, 1998.

[36] R. Ramírez, T. Pöschel, N. V. Brilliantov, and T. Schwager. Coefficient of restitution of cooling viscoelastic spheres. *Phys. Rev. E*, 60:4465–4472, 1999.

[37] F. Gerl and A. Zippelius. Coefficient of restitution for elastic disks. *Phys. Rev. E*, 59:2361–2372, 1999.

[38] H. Kuninaka and H. Hayakawa. The impact of two-dimensional elastic disk. *J. of Phys. Soc. Jpn.*, 70:2220–2221, 2001.

[39] H. Hayakawa and H. Kuninaka. Simulation and theory of the impact of two-dimensional elastic disks. *Chem. Eng. Sci.*, 57:239–252, 2002.

[40] H. Hayakawa and H. Kuninaka. Simulation of the impact of two-dimensional elastic disks. In *The proceedings of the ninth nisshin engineering particle technology international symplsium*, pages 82–95, 2001.

[41] H. Hayakawa and H. Kuninaka. Coefficient of restitution of elastic disks. In Y. Kishino, editor, *The proceedings of powders and grains 2001*, pages 561–564. Rotterdam: Balkema, 2001.

[42] C. E. Smith and Pao-Pao Liu. Coefficients of restitution. *J. of Appl. Mech.*, 59:963–969, 1992.

[43] J. Calsamiglia, S. W. Kennedy, A. Chatterjee, A. Ruina, and J. T. Jenkins. Anomalous frictional behavior in collisions of thin disks. *J. of Appl. Mech.*, 66:146–152, 1997.

[44] A. Chatterjee. *RIGID BODY COLLISIONS: SOME GENERAL CONSIDERATIONS, NEW COLLISION LAWS, AND SOME EXPERIMENTAL DATA*. PhD thesis, Cornell University, 1997.

[45] G. Kuwabara, H. Tanaka, and K. Kono. Splash produced by a smooth sphere od circular cylinder striking a liquid surface. *J. Phys. Soc. Jpn.*, 56:2733–2743, 1987.

[46] P. Aussillous and D. Quéré. Liquid marbles. *Nature*, 411:924–927, 2001.

[47] K. Tanaka, M. Nishida, T. Kunimochi, and T. Takagi. Discrete element simulation and experiment for dynamic response of two-dimensional granular matter to the impact of a spherical projectile. *Powder. Tech.*, 124:160–173, 2002.

[48] H. Hertz. Über die beruhrung fester elastische körper. *J. Reine Angew. Math.*, 92:156–171, 1882.

[49] L. D. Landau and E. M. Lifshitz. *Theory of Elasticity (2nd English ed.)*. Pergamon, 1960.

[50] A. E. H. Love. *A Treatise on the Mathematical Theory of Elasticity*. Cambridge Univ. Press, 1927.

[51] D. A. Hills, D. Nowell, and A. Sackfield. *Mechanics of Elastic Contacts*. Butterworth-Heinemann, Oxford, 1993.

[52] R. D. Mindlin. Compliance of elastic bodies in contact. *Trans. ASME, J. Appl. Mech.*, 16:259–268, 1949.

[53] R. D. Mindlin and H. Deresiewicz. Elastic spheres in contact under varying oblique forces. *Trans. ASME, J. Appl. Mech.*, 20:327–344, 1953.

[54] H. Hayakawa and H. Kuninaka. Theory of inelastic impact of elastic materials. *Phase Transision.* (to be published).

[55] O. M. Rayleigh. On the prediction of vibrations by force of relatively long duration, with application to the theory of collisions. *Philos. Mag. Ser. 6*, 11:283–292, 1906.

[56] G. F. Miller and H. Pursey. The field and radiation impedance of mechanical radiators on the free surface of a semi-infinite isotropic solid. *Proc. Roy. Soc.*, A 223:521–541, 1954.

[57] G. F. Miller and H. Pursey. On the partition of energy between elastic waves in a semi-infinite solid. *Proc. Roy. Soc.*, A 233:55–69, 1955.

[58] S. C. Hunter. Energy absorbed by elastic waves during impact. *J. Mech. Phys. Solids*, 5:162–171, 1957.

[59] G. Giese and A. Zippelius. Collision properties of one-dimensional granular particles with internal degrees of freedom. *Phys. Rev. E*, 54:4828–4837, 1996.

[60] T. Aspelmeier, G. Giese, and A. Zippelius. Cooling dynamics of a dilute gas of inelastic rods: A many particle simulation. *Phys. Rev. E*, 57:857–865, 1998.

[61] S. Nagahiro and Y. Hayakawa. Statistical-mechanical study of the collision between a crystal lattice and a rigid wall. *Phys. Rev. E*, 67:036609–1–036609–6, 2003.

[62] M. Sugiyama and N. Sasaki. Statistical-mechanical study of the collision between a crystal lattice and a rigid wall. *J. Phys. Soc. of Jpn.*, 68:1859–1863, 1999.

[63] A. G. Basile and R. S. Dumont. Coefficient of restitution for one-dimensional harmonic solids. *Phys. Rev. E*, 61:2015–2023, 2000.

[64] E. Falcon, C Laroche, S. Fauve, and C. Coste. Collision of a 1-d column of beads with a wall. *Eur. Phys. J. B*, 5:111–131, 1998.

[65] C. T. Lim and W. J. Stronge. Normal elastic-plastic impact in plane strain. *Math. Compt. Modelling*, 28:323–340, 1998.

[66] H. Minamoto. Simulation for collisions of spheres using ls-dyna (in japanese). In *Proceedings of Supercomputer Symposium 2002 (Osaka University, Japan)*, 2002.

[67] C. Wu, L. Li, and C. Thornton. Rebound behavior of spheres for plastic impacts. *Int. J. Imp. Eng.*, 28:929–946, 2003.

[68] A. Norton, G. Turk, B. Bacon, J. Gerth, and P. Sweeney. Animation of fracture by physical modeling. *Visual Computer*, 7:210–219, 1991.

[69] Y. Hayakawa. Numerical study of oscillatory crack propagation through a two-dimensional crystal. *Phys. Rev. E*, 49:R1804–R1807, 1994.

[70] Y. Hayakawa. Pattern selection of multicrack propagation in quenched crystals. *Phys. Rev. E*, 50:R1748–R1751, 1994.

[71] W. G. Hoover. *Computational Statistical Mechanics*. Elsevier Science, Amsterdam, 1991.

[72] H. Kuninaka. The analysis of the coefficient of restitution for the two-dimensional elastic disk. Master's thesis, Kyoto University, 2000.

[73] H. Kuninaka and H. Hayakawa. Simulation of the impact of two-dimensional elastic disks. In M. Fukui, Y. Sugiyama, M. Schreckenberg, and D. E. Wolf, editors, *The proceedings of Traffic and Granlar Flow 2001*, pages 467–472, Berlin, 2003. Springer.

[74] H. Kuninaka and H. Hayakawa. The anomalous behavior of coefficient of restitution in the oblique impact. preprint(submitted to Phys. Rev. Lett.).

[75] K. Sugihara. *Data Structure and Algorithms(in Japanese)*. Kyoritsu, Japan, 2001.

[76] J. Schäfer, S. Dippel, and D. E. Wolf. Force schemes in simulations of granular materials. *Phys. Rev. E*, 52:4442–4457, 1995.

[77] C. Zener. The intrinsic inelasticity of large plates. *Phys. Rev.*, 59:669–673, 1941.

[78] L. A. Galin. *Contact problems in the theory of elasticity*. Gostekhizdat, Moskow, 1953.

[79] H. Kuninaka and H. Hayakawa. Simulation for the oblique impact of a lattice system. *J. Phys. Soc. Jpn.*, 72:1655–1663, 2003.

[80] S. Luding. Granular materials under vibration: Simulations of rotating spheres. *Phys. Rev. E*, 52:4442–4457, 1995.

[81] S. Luding. Collisions and contacts between two particles. In H. J. Hermmann, J. P. Hovi, and S. Luding, editors, *Physics of dry granular media*, pages 285–304, Dordrecht, 1998. Kluwer academic publishers.

[82] R. P. Feynman, R. B. Leighton, and M. Sands. *Lectures on Physics Vol. 2*. Addison-Wesley, Reading, MA, 1964.

List of Publication

Reviewed papers

1. H. Kuninaka and H. Hayakawa:
   ”The impact of two-dimensional elastic disks”
   J. Phys. Soc. Jpn **70** (2001) 2220

2. H. Hayakawa and H. Kuninaka:
   ”Simulation and theory of the impact of two-dimensional elastic disks”
   Chem. Eng. Sci. **57** (2002) 239

3. H. Kuninaka and H. Hayakawa:
   ”Simulation of the Impact of Two-dimensional Elastic Disks”
   Traffic & Granular Flow 2001, (2003) p.p. 467
   (Berlin: Springer, eds. by M. Fukui, Y. Sugiyama, M. Schreckenberg, and D. E. Wolf)

4. H. Kuninaka and H. Hayakawa:
   ”Simulation for the Oblique Impact of a Lattice System”
   J. Phys. Soc. Jpn **72** (2003) 1655

5. H. Kuninaka and H. Hayakawa:
   ”The anomalous behavior of coefficient of restitution in the oblique impact”
   (submitted to Phys. Rev. Lett.)

6. H. Hayakawa and H. Kuninaka:
   ”Theory of the inelastic impact of elastic materials”
   Phase Transitions (to be published)

7. H. Kuninaka and H. Hayakawa:
   ”The Simulation of Inelastic impact”
   The proceedings of the 3rd International Symposium on Slow Dynamics in Complex Systems
   (to be published in AIP conference proceedings, eds. by M. Tokuyama and I. Oppenheim)

Others

1. H. Hayakawa and H. Kuninaka:
   ”Simulation of the Impact of Two-dimensional Elastic Disks”
   The proceedings of 9th Nisshin engineering particle technology international symposium (2001) p.p. 82

2. H. Hayakawa and H. Kuninaka:
   ”Coefficient of restitution of elastic disk”
   Powders & Grains 2001 (2001) p.p. 561
   (edited by Y. Kishino, 2001, Rotterdam: Balkema)